Pharmaceutical Research
https://doi.org/10.1007/s11095-025-03906-3

REVIEW ARTICLE

Numerical Investigation to Improve Pulmonary Drug Delivery via Dry Powder Inhalers: A Review of *In-Silico* Modeling

Salar Salmanipour[1,2] · Sasan Salmani Pour Avval[3] · Kiao Inthavong[4] · Hamed Hamishehkar[2,5]

Received: 21 June 2025 / Accepted: 26 July 2025

Abstract

This review focuses on the application of computational fluid dynamics (CFD) in pulmonary drug delivery, particularly for treating asthma and COPD with pharmaceutical aerosols via dry powder inhalers (DPIs). Aerosol drug delivery effectiveness relies on accurate assessment and prediction of particle deposition in the respiratory system. This method is crucial due to the high number of pulmonary disease cases, efficient lung absorption capabilities, lower dosage required, and reduced systemic side effects compared to oral medications. Given the limits of *in vivo* and *in vitro* methods, CFD modeling has advanced rapidly over 20 years, especially when combined with discrete phase model (DPM) and discrete element method (DEM) approaches. CFD simulations can correctly account for a wide range of realistic or idealized parameters using numerical solutions of particle and airflow transport equations. Achieving accurate simulations requires avoiding simplifications and approximating real-world conditions, which will soon be more possible with advancing computing tools. The research aims to review numerical modeling of pulmonary drug delivery along the mouth-to-lung pathway, encompassing governing equations, forces, boundary conditions, the influence of lung geometry on CFD modeling, the effects of powder characteristics on aerosolization and pulmonary deposition, validation of computational results with *in vitro*/*in vivo* data, and a discussion of current challenges and future prospects.

Keywords computational fluid dynamics (CFD) · human respiratory system · inhalation therapy · numerical modeling · pulmonary drug delivery systems

Introduction

Inhaled micron- and nanosized particulate matter, primarily from air pollution (e.g., fossil fuel combustion and microplastics), can penetrate deep into the respiratory tract [1–3]. Depending on their residence time, composition, and toxicity, these particles may cause conditions such as asthma and chronic obstructive pulmonary disorder (COPD) [4]. Upon inhalation, pollutants may dissolve in epithelial cells or persist as aerosols, potentially damaging airway tissue and triggering inflammation, stiffness, and obstruction [5].

Aerosols have long served as effective carriers for respiratory therapeutics, with historical practices like inhaling plant smoke illustrating early use [6]. Inhalation offers several advantages: (i) rapid absorption, (ii) suitability for poorly absorbable drugs (e.g., peptides), (iii) reduced dosage, and (iv) fewer systemic side effects [7–9]. However, efficient aerosol delivery depends on factors such as device type, airway anatomy, inspiratory maneuvers, and particle

Salar Salmanipour and Sasan Salmani Pour Avval participate equally as the first author.

✉ Kiao Inthavong
kiao.inthavong@rmit.edu.au

✉ Hamed Hamishehkar
hamishehkarh@tbzmed.ac.ir;
hamishehkar.hamed@gmail.com

1 School of Chemical Engineering, College of Engineering, University of Tehran, Tehran, Iran

2 Drug Applied Research Center, Tabriz University of Medical Sciences, Tabriz, Iran

3 Faculty of Aerospace Engineering, Delft University of Technology, Delft, Netherlands

4 Mechanical Manufacturing Mechatronic Engineering, RMIT University, PO Box 71, Bundoora, VIC 3083, Australia

5 Research Center of New Material and Green Chemistry, Khazar University, 41 Mehseti Street, AZ1096 Baku, Azerbaijan

Published online: 15 August 2025

properties—considerations that became especially critical during the COVID-19 pandemic [10].

Most recent CFD studies in this area fall into two broad subcategories (Fig. 1): (1) the design and optimization of respiratory devices for improved performance [11], and (2) airway deposition modeling for more effective drug delivery and treatment. This section focuses on the latter, specifically lung simulations via the mouth-throat pathway, excluding nasal sprays and targeted nasal aerosols.

CFD, a branch of fluid mechanics, uses numerical methods to simulate fluid flow and predict behavior under varying conditions [12]. Initially applied to study inhaled substances like coal dust and smoke, lung deposition models have advanced with improved understanding of respiratory physiology and multiphase flow. These simulations are now vital for analyzing aerosol deposition and ensuring effective pulmonary drug delivery [13]. CFD offers precise spatial and temporal simulations for respiratory drug delivery [14]. Studies show that most aerosol particles deposit in the upper airways, while current inhalers struggle to reach deeper regions [15]. Inefficient deposition in the mouth-throat area can cause side effects. Improving delivery efficiency—from 25 to 90%—requires understanding air-particle dynamics, dissolution, absorption, and mucociliary clearance. Drug distribution depends on formulation, inhalation conditions, and device type [16]. Among delivery systems—DPIs, pressurized metered-dose inhalers (pMDIs), soft mist inhalers (SMIs), and nebulizers—DPIs are superior in stability, bioavailability, ease of use, and propellant-free design [17].

Aerosol deposition in human airways can be assessed *in vivo*, *in vitro*, or *in silico*. *In vivo* methods are common but limited by high imaging costs, time-intensive aerosol labeling, technical challenges, resolution limits, and radiation risks [18, 19]. *In vitro* methods use airway replicas

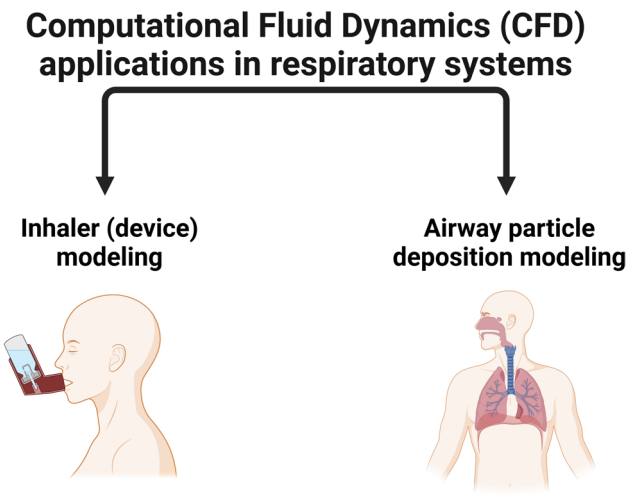

Fig. 1 The two key objectives of pulmonary drug delivery analysis via CFD are to enhance device design and improve drug deposition in airways for better treatment.

to study deposition but are costly and lack detail, limiting their use in small anatomical regions [20]. In contrast, *in silico* techniques enable efficient, safe analysis of aerosol dynamics in inaccessible lung areas by integrating geometry, breathing patterns, and particle properties into CFPD models [21]. Their clinical relevance and practicality have driven a sharp rise in CFD-based aerosol research over the past two decades.

CFD is a powerful tool for simulating fluid motion and drug transport within the lungs. This study aims to investigate pulmonary drug delivery using CFD to enhance localized deposition. It involves examining airflow and drug transport simulations from the oral cavity to lung regions, while considering factors such as boundary and initial conditions that influence fluid dynamics and mass transfer. Additionally, we address lung anatomy and imaging techniques, including computed tomography (CT) and magnetic resonance imaging (MRI), for constructing realistic or idealized three-dimensional lung models. We also review the properties of drug powders that impact deposition, aerosolization, and flow behavior. Tables II and III provide a summary of recent CFD studies on pulmonary drug delivery. Finally, we evaluate methods for validating simulation outcomes using *in vitro* and *in vivo* data.

Pulmonary Drug Delivery Modeling

Governing Equations, Forces, and Boundary Conditions

Numerical Modeling from Mouth to Lung Pathway

Mouth breathing delivers air more effectively during physical exertion or medical conditions. Due to higher filtration in the nasal pathway, aerosol drugs are preferably administered orally to enhance lung penetration—the primary goal of drug delivery [15, 22]. Although devices like DPIs, pMDIs, and SMIs are affordable and adaptable, the fine particle fraction (FPF) they emit represents only 20–40% of the total FPF for inhalers and 0.5–12% for nebulizers [23, 24], reflecting limited efficiency—particularly concerning for high-cost drugs. CFD models effectively apply conservation laws of mass, momentum, and energy to simulate fluid and particle flows. This non-invasive, cost-efficient method supports the analysis of aerosol conditions, delivery techniques, and airway geometries without relying on empirical correlations [25]. Micron-sized particles often act as gas tracers, avoiding deposition or being exhaled. In contrast, aerosols deposited in the mouth-throat region fail to reach target zones and may cause side effects [26, 27]. Accurate *in silico* predictions of regional aerosol deposition [28] can enhance treatment strategies, patient care, and diagnosis.

Numerical techniques—finite difference method (FDM), finite element method (FEM), and finite volume method (FVM)—convert differential equations into algebraic systems, enabling the solution of non-linear partial differential equations that lack analytical solutions. This involves discretizing geometry and applying methods like Taylor series expansion to approximate spatial and temporal derivatives. Open-source software such as OpenFOAM [29] provides customization and parallel processing, while commercial tools like ANSYS Fluent [5], ANSYS CFX [30], COMSOL Multiphysics, and STAR-CCM + [31] can be used for performing the computations.

Air Flow

Identifying airflow type is key in simulations of respiratory dynamics. Breathing's cyclic nature induces unstable flow due to constant pressure fluctuations. Computational fluid dynamics studies show turbulent flow in the middle and upper tracheobronchial (TB) airways, intensified by jets from the 6mm-diameter DPI aperture and glottis [17, 32, 33]. Accurate flow prediction requires appropriate turbulence models and mesh resolution [34]. Airway branching and diameter reduction decrease Reynolds number, likely due to anatomical complexity. Even at modest inhalation rates, flow may be fully turbulent in extra-thoracic airways and shift through turbulent, transitional, and laminar regimes deeper in the lungs [16, 35]. In the alveoli, flow may become creeping with Poiseuille-like velocity profiles [36]. In DPIs, shear forces from inhaled airflow disperse powder into aerosols, highly dependent on inhalation strength. Peak inspiratory flow rates of 15, 30, and 60 l/min correspond to sedentary, light, and heavy activity levels [37]. Medicinal inhalation devices can induce rates up to 120 L per minute. Higher flow rates trigger early turbulence in upper airways, leading to erratic aerosol motion and size-dependent deposition shifts [38]. The Reynolds number indicates flow regime by comparing inertial and viscous forces. It decreases in deeper airways due to reduced cross-sectional area, as shown in Fig. 2.

Studies show that particles between $0.5-1\,\mu m$ are mostly exhaled, while those between $1-5\,\mu m$ remain airborne and settle early in exhalation [29]. This supports brief breath-holding post-inhalation to enhance deep lung deposition. Turbulence models simulate the chaotic airflow patterns during breathing, capturing transient and turbulent dynamics, as illustrated in Fig. 3.

DPI simulations often employ Reynolds-Averaged Navier–Stokes (RANS) equations to model turbulent flows due to their robustness and low computational cost compared to Direct Numerical Simulation (DNS) and Large Eddy Simulation (LES). RANS models approximate turbulent fluctuations using empirical data from canonical

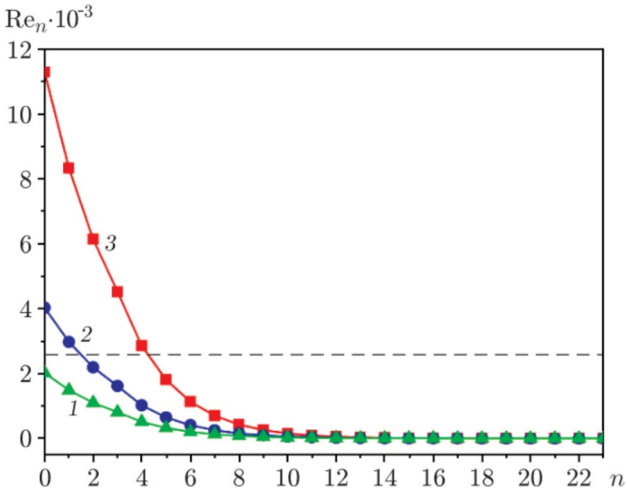

Fig. 2 Reynolds number *versus* the bifurcation number for different air flow rates: Q = 25 (1), 50 (2), and 140 l/min (3); the dashed line shows the critical Reynolds number for a circular tube (Re = 2300). Reprinted from Medvedev et al. [39], with permission from Elsevier.

flows. Capturing laminar-turbulent-laminar transitions in airways requires careful model selection. RANS decomposes instantaneous velocity into mean flow and time-dependent turbulence fluctuations. The standard k-ε and k-ω [40, 41] formulations represent prevalent RANS approaches that establish a correlation between the Reynolds stress and the turbulent kinetic energy (k), as well as its dissipation rate (ε) or the specific rate of turbulent dissipation (ω) [20]. They are sometimes referred to as two-equation RANS models as the two turbulence parameters, k and ε or k and ω, are solved by two extra transport equations. Like the k-ω model, the k-ε model can be appropriate for specific lung segments but not others, and vice versa [42, 43]. Most of the issues with the k-ε model are thought to be related to the ε equation. The realizable k-ε turbulence model, superior to the standard variant, effectively simulates turbulence across diverse conditions such as rotating homogeneous shear, boundary-free shear flows, and channel and flat plate boundary layers with varying pressure gradients [31, 44–46]. Due to the complexity of the flow field, advanced turbulence models beyond standard k-ε or k-ω are required. The SST model blends k-ω near walls and k-ε in free-stream regions, offering resilience, ease of use, and improved performance in non-equilibrium boundary layers [5, 10, 23, 42, 47–50]. Although computationally demanding and grid-sensitive, Reynolds-stress models (RSM) effectively capture anisotropic turbulence, including reversed flows and secondary vortices, by solving six Reynolds stress transport equations plus one for dissipation [51, 52].

LES is a high-fidelity, resource-intensive method that outperforms RANS in predicting velocity profiles, especially in transitional flows. This enhanced accuracy is achieved by directly resolving the dynamics of the larger eddies through

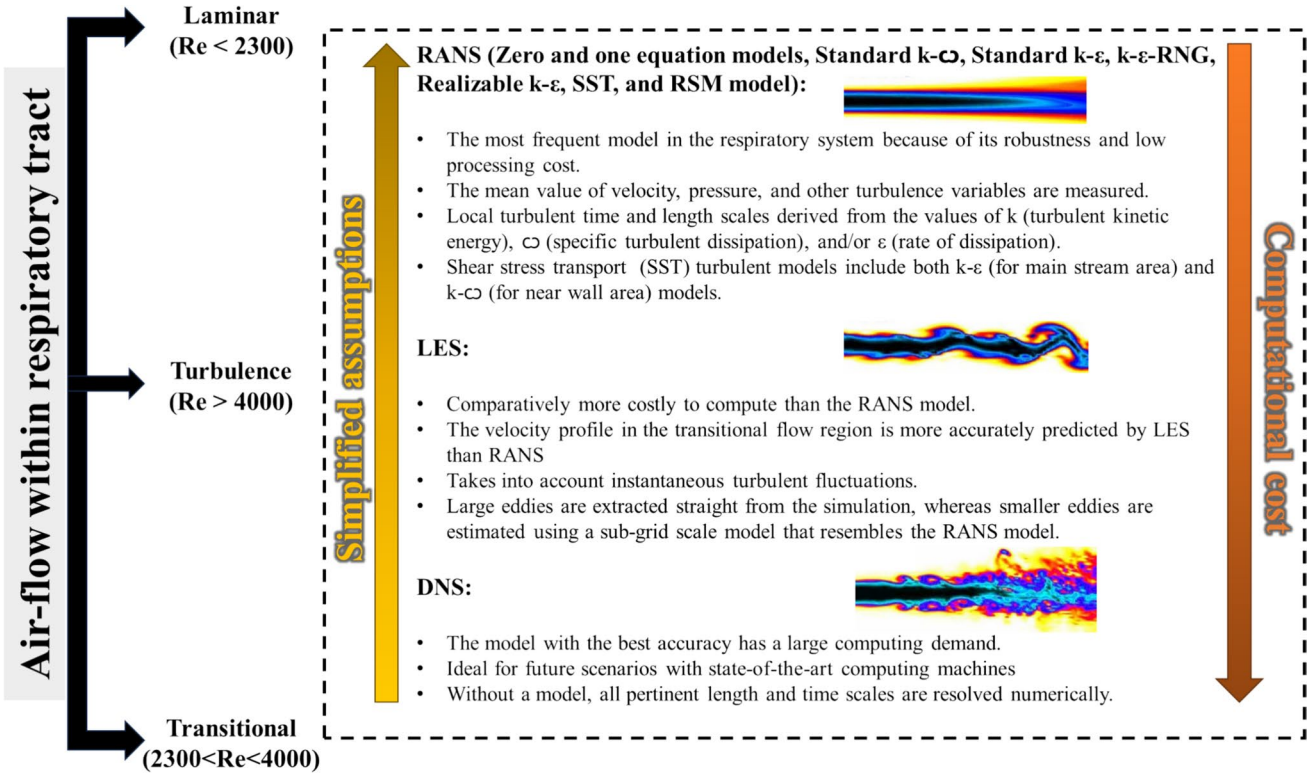

Fig. 3 Dynamics of air circulation in the respiratory tract: A comparison of distinct turbulence models and their key features.

simulation, while the effects of the smaller eddies are addressed by employing low-pass filtering. The resultant flow behaviors of these smaller scales are then approximated using subgrid-scale models, employing methodologies akin to those used in RANS [38, 53–58].

Improving aerosol deposition accuracy requires shifting from RANS and LES to high-fidelity approaches like DNS, which avoid empirical assumptions. DNS enables detailed insight into turbulence attenuation across airway generations—a key step for future research. However, its application to lung aerosol dynamics is constrained by extreme computational demands as it necessitates the numerical resolution of all pertinent length and time scales, particularly within intricate flow domains like the respiratory system. Consequently, its practicality for such applications remains limited [53, 59].

CFD models intricately compute airflow fields exhibiting laminar and turbulent behaviors by numerically solving the Navier–Stokes equations. These equations conceptualize the fluid as a continuum and calculate flow dynamics such as velocity and pressure through the laws of mass and momentum conservation as follows:

Continuity equation:

$$\frac{\partial(u_j)}{\partial x_j} = 0, \tag{1}$$

Navier–Stokes equation:

$$\frac{\partial u_i}{\partial t} + (u_j)\frac{\partial u_i}{\partial x_j} = -\frac{1}{\rho}\frac{\partial p}{\partial x_i} + \frac{1}{\rho}\frac{\partial \tau_{ij}}{\partial x_j} + g_i \tag{2}$$

The symbols u, ρ, p, τ, t, x and g correspond to the velocity of the fluid, the density of the fluid, the pressure within the fluid, the viscous stress tensor, the temporal variable, the spatial variable, and the acceleration due to gravity, respectively.

The viscous stress tensor is given by:

$$\tau_{ij} = \mu[(\frac{\partial u_i}{\partial x_j} + \frac{\partial u_j}{\partial x_i}) - \frac{2}{3}\delta_{ij}\frac{\partial u_k}{\partial x_k}] \tag{3}$$

Within the context of the RANS turbulence model, the equation originally referred to as the Navier–Stokes equation is more accurately described as the Reynolds-averaged Navier–Stokes (RANS) equation.

Reynolds-averaged Navier–Stokes (RANS) equation:

$$\frac{\partial(\rho\overline{u_i})}{\partial t} + \frac{\partial(\rho\overline{u_i u_j})}{\partial x_j} = -\frac{\partial \overline{p}}{\partial x_i} + \frac{\partial}{\partial x_i}\left[\mu\left(\frac{\partial \overline{u_i}}{\partial x_j} + \frac{\partial \overline{u_j}}{\partial x_i}\right)\right] + \frac{\partial}{\partial x_j}\left(-\rho u_i' u_j'\right) + \rho g_i \tag{4}$$

where the fluctuation component of the velocity is denoted by u' and the time-average velocity component by $\overline{u}$. $\overline{p}$ represents modified time-averaged pressure term. In Eq. (4), the expression $-\rho u_i' u_j'$ represents the turbulent Reynolds stresses which should be expressed as mean flow quantities. Subsequent to the formulation of the RANS equations, Boussinesq proposed the eddy viscosity (μ_t) notion, which

simplifies the Reynolds stress tensor, facilitating the resolution of these equations. Additional equations for k, ω and/or ε used to find the eddy viscosity ($\mu_t = f\left(\frac{\rho k}{\omega}\right) or f\left(\frac{\rho k^2}{\varepsilon}\right)$) for Reynolds stresses calculation and finally solving the RANS equations [30, 40, 60–63].

On the other hand, according to Smagorinsky's model, the Navier–Stokes equation for LES model represented by [38, 55, 56, 64, 65]:

$$\frac{\partial(\overline{u_i})}{\partial t} + \frac{\partial(\overline{u_i u_j})}{\partial x_j} = -\frac{1}{\rho}\frac{\partial \overline{p}}{\partial x_i} + \frac{\partial}{\partial x_i}\left[\upsilon\left(\frac{\partial \overline{u_i}}{\partial x_j} + \frac{\partial \overline{u_j}}{\partial x_i}\right) - \tau_{ij}^r\right] + g_i \tag{5}$$

where τ_{ij}^r is the sub-grid scale stress tensor as follows:

$$\tau_{ij}^r = -2C_s\Delta^2\left|\overline{S}\right|\overline{S_{ij}} \tag{6}$$

where C_s is the Smagorinsky constant and $\Delta = (\Delta x \Delta y \Delta z)^{\frac{1}{3}}$ is the filter width. The strain rate tensor ($\overline{S_{ij}}$) and $\left|\overline{S}\right|$ are shown as:

$$\overline{S_{ij}} = \frac{1}{2}\left(\frac{\partial \overline{u_i}}{\partial x_j} + \frac{\partial \overline{u_j}}{\partial x_i}\right) \tag{7}$$

$$\left|\overline{S}\right| = \sqrt{2\overline{S_{ij}}\overline{S_{ij}}} \tag{8}$$

Velocity and pressure profiles derived from the aforementioned relationships provide key insights for enhancing pulmonary drug delivery [42]. Increased flow rates elevate particle DF via inertial impaction, especially for 2.5 and 5 µm particles in the mouth-throat region. In contrast, smaller particles (0.1–1 µm) show minimal DF variation with flow rate [38]. Koullapis et al. demonstrated that deep inhalation markedly improves deposition in the respiratory zone by minimizing upper airway losses. Breath-holding further boosts deposition by ~ 70% for 1–2 µm particles. For optimal targeting, deep inhalation plus breath-holding enhances delivery to the respiratory zone, whereas gentle breathing with breath-holding favors the lower conducting airways [66]. Chalvatzaki et al. showed that breath-holding enhances lung deposition across various mouthpiece sizes and MMADs, supporting clinical recommendations for post-inhalation breath-holding with DPIs [67]. Rahman et al. found age-related increases in airway velocity due to narrowed airways, with septuagenarians exhibiting 27.62% higher pressure in G3–G6 than quinquagenarians when G15 exit pressure is zero [45]. Islam et al. investigated low-density heliox mixtures to minimize upper airway deposition. Compared to air, heliox produced smoother flow, lower turbulence intensity, and reduced deposition efficiency in the upper airways, while air inhalation generated ~ 4.7 × higher pressure across inlet conditions [15].

In pulmonary CFD analyses, primary and secondary vortices critically influence airflow patterns and particulate transport. Intensified secondary vortices increase deposition in the upper respiratory tract [55]. These smaller whirls form within larger swirls, interacting with the main flow and altering its trajectory. Their emergence is driven by complex airway geometry, flow-wall interactions, and dichotomous branching. Advanced airway generations show velocity deviations due to duct intricacies, flow separation, and secondary vortex formation. Minor structural changes can trigger these vortices, whereas higher flow rates tend to suppress them [52]. Cui et al. found that light breathing at 15 L/min produces steadier flow with longer, concave laryngeal jets and more secondary vortices, reducing particle–wall interactions. In contrast, heavy breathing destabilizes the jet and intensifies its interaction with the trachea's recirculation zone, increasing particle entrainment, dwell time, and deposition in the trachea. Secondary vortices arise post-glottis during gentle breathing, but from the pharynx during forceful inhalation, with a higher vortex count in the trachea under intense flow [55]. Cui et al. identified 3D vortical structures in both transient and averaged flow fields across oral, pharyngeal, laryngeal, and tracheal regions, as well as the pharyngeal recirculation zone. In steady flow, tongue and glottal obstructions respectively induce hairpin and horseshoe vortices. Vortex dynamics become more complex in unsteady flows, with higher flow rates producing more frequent, smaller vortices in the trachea [56]. Ahookhosh et al. found that turbulence, reverse flow, vortex generation, and the laryngeal jet heavily impact airflow and particle deposition in the extra-thoracic region. Deposition is highest in the mouth-throat due to turbulence at the soft palate and vortex formation in the oral cavity and oropharynx, with the laryngeal jet driving high deposition in the upper trachea [60].

Particles Behaviors and Interactions

Predicting aerosol transport within human lungs helps pinpoint toxin accumulation zones and optimize parameters for drug delivery and inhaler design. Accurate modeling of localized deposition is essential for improving treatment outcomes. For nano/micro particle dynamics, Eulerian–Eulerian (E–E) and Eulerian–Lagrangian (E–L) frameworks are commonly employed (Fig. 4). Fluid flow is typically resolved using an Eulerian approach, while particle motion can be described either Eulerianly or Lagrangianly—the latter is preferred for DPI applications due to its ability to track individual particle trajectories over time. Unlike the Eulerian approach, which observes particle flow at fixed spatial points, the Lagrangian method follows particles through space and time, enabling detailed motion analysis. The Eulerian–Lagrangian (E–L) method assumes the secondary phase occupies a smaller volume than the primary and

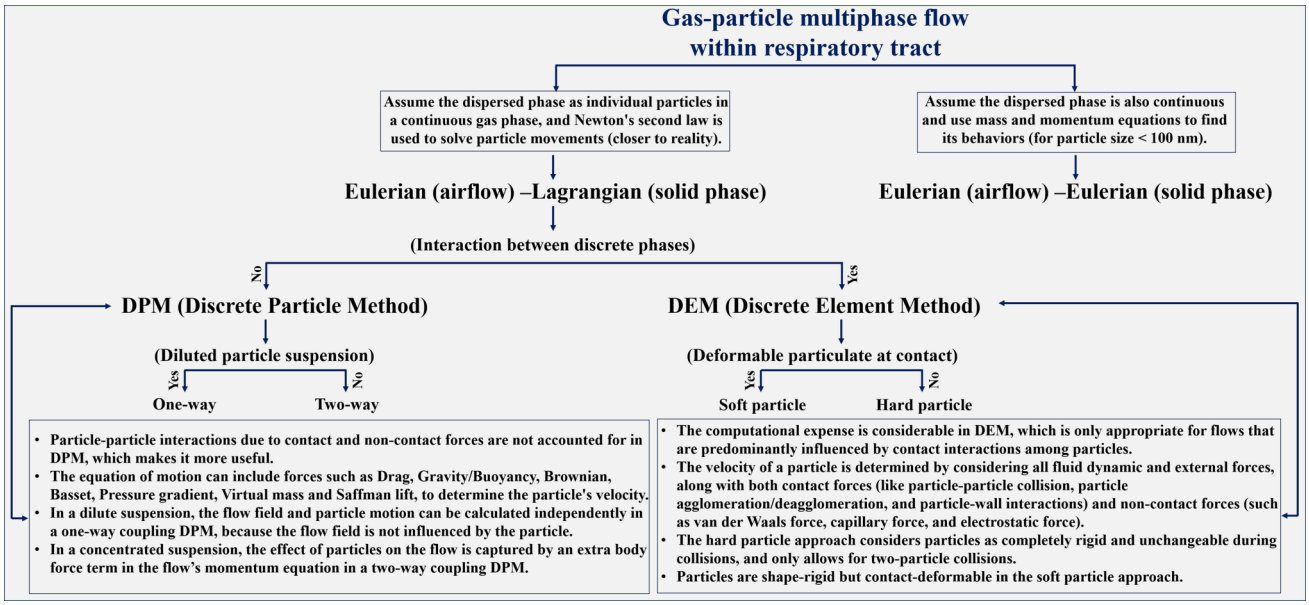

Fig. 4 Analysis of aerosol particle movement in the respiratory system through Eulerian–Lagrangian methods (DPM and DEM) and the Eulerian-Eulerian framework.

tracks particles individually by integrating Newton's second law over time [68, 69]. This approach, treating aerosols as discrete particles in a continuous gas phase, offers intuitive modeling of turbulent dispersion and particle–wall interactions [20]. In contrast, the Eulerian–Eulerian (E–E) method handles both phases as interpenetrating fields and predicts particle behavior via mass and momentum equations, without accounting for inertia [70, 71]. E–E is more suitable for particles ≤ 100 nm, where inertial effects are minimal and E–L's advantages are less pronounced [72].

Advances in computational technologies have made CFD modeling—particularly when integrated with discrete phase model (DPM) and discrete element method (DEM)—a vital tool for predicting airflow behavior, including turbulence, particle trajectories, deagglomeration in DPIs, and aerosol delivery to the lungs. Accuracy depends on whether the Lagrangian model incorporates interactions between discrete phases [20]. These methods must consider forces acting on particles, influenced by particle size, fluid-to-particle density ratio, and flow conditions.

Understanding the factors influencing pulmonary particle deposition is essential for assessing both therapeutic potential and toxicological risks. Most models omit pressure gradient and Basset forces, relying primarily on drag and gravity [73, 74]. In distal airway generations, increased angular variability relative to gravity substantially affects deposition, especially for particles > 2 µm [29]. For submicron particles in laminar flow, Brownian motion—caused by random bombardment from the continuous phase—plays a significant role and is modeled as a Gaussian white noise force [53, 75]. The virtual mass force becomes relevant when the carrier-phase density far exceeds that of the particle, adding inertia as the particle moves through the fluid, though its impact in pulmonary drug delivery is minimal [52]. For micron-sized particles, most additional forces—such as Saffman's lift, buoyancy, pressure gradient, Basset force, Brownian motion, and virtual mass—are negligible, allowing models to prioritize dominant forces for simplified dynamics.

Particle collisions in the DPM are binary and instantaneous, indicating their extremely brief duration relative to other time scales. Particle velocities are updated via Newton's second law [76]. Lagrangian simulations are widely used to predict particle dispersion in DPI systems due to their simplicity and ability to approximate particle trajectories. The model assumes particle motion is governed by gravity, flow-induced forces, and wall collisions. Flow-related forces typically include drag, pressure gradient, added mass, Basset, and lift. Model accuracy depends on the selected forces and empirical correlations, derived either from flow field data or established relationships. However, DPM cannot simulate particle–particle interactions like deformation, adhesion, or de-agglomeration, limiting its suitability for simulations requiring such detailed dynamics. DPM employs either one-way or two-way coupling. One-way coupling neglects particle influence on the flow, while two-way coupling accounts for it by adding a body force term to the flow's momentum equation [71, 77]. At high particle concentrations—such as those released from capsules—two-way coupling becomes essential, as collective particle effects can significantly alter flow dynamics. However, most Computational Fluid Dynamics-Discrete Phase Model (CFD-DPM) studies on respiratory aerosol transport assume a dilute dispersed phase.

One-way coupling assumes particles exert negligible influence on airflow, rendering inter-particle interactions non-essential [5, 78]. In contrast, Lagrangian CFD-DEM—like DPM—follows Newton's second law but enables multi-particle interactions, making it suitable for contact-dominated flows. It effectively captures agglomeration and de-agglomeration dynamics [24].

Introduced by Cundall and Strack in fluidized bed simulations, DEM applies Newton's laws to govern each particle's translational and rotational motion [79]. It offers superior accuracy in modeling particle behavior, especially in interaction-dominant systems like concentrated dry powders. However, DEM is computationally far more intensive than DPM and requires extensive pre-simulation experimental data. Particle contact forces in dynamics are modeled via hard or soft particle approaches. The hard model treats particles as rigid and permits only binary collisions. The soft model allows deformation upon contact—termed overlapping—and supports multi-particle interactions. Forces involved include mechanical contact, van der Waals, capillary, and electrostatic forces, acting either through contact or at a distance [80]. Electrostatic charge significantly influences particle deposition in the respiratory tract, especially in drug delivery. Devices like nebulizers, MDI, and DPI generate charged aerosols, and environmental aerosols may carry charges exceeding Boltzmann equilibrium levels [81, 82]. Electrostatic effects must be considered in health risk assessments. Relative humidity (RH) plays a critical role by modulating charge strength, drug deposition, triboelectric charging in DPIs, and aerosolization efficiency. Generally, charge intensity decreases as RH increases. However, the mechanisms governing electrostatic charging and RH effects in pharmaceutical aerosols remain poorly understood [82–85]. Koullapis et al. found that electrostatic charge can enhance DF of smaller particles by up to sevenfold, especially in the mouth-throat region due to its large surface area and complex airflow. For particles > 2.5 µm, inhalation rate had limited impact, with impaction dominating deposition as flow increased. These findings suggest that tuning electrostatic charge may optimize particle deposition in the conducting airways [38]. Using DEM-CFD, Ohsaki et al. examined how particle dynamics and morphology influence deposition in the lungs. Smaller, lighter particles with favorable aerodynamic diameters penetrated deeper into a simplified lung model. The study highlighted the roles of particle–wall interactions and shape in deposition patterns, with contact forces computed via the JKR (Johnson-Kendall-Roberts) theory, a widely accepted model for adhesion effects [41].

The Lattice Boltzmann Method (LBM) models fluid density via streaming and collisions on a lattice, contrasting with conventional CFD approaches that solve the Navier–Stokes equations using macroscopic variables like velocity and pressure. Traditional methods employ finite element, finite difference, or finite volume techniques, while LBM computes flow properties by tracking distribution function momentum at a microscopic scale. Cui and Sommerfeld introduced a method to evaluate drug powder detachment from carrier particles, critical for DPIs subjected to intense turbulence. LBM was used to model fluid dynamics in clusters containing 100 µm carriers and 5 µm spherical drug particles at 50% coverage, totaling 882 particles. Detachment probabilities via lift-off, sliding, or rolling were assessed based on measured adhesive forces and surface energy characteristics [86–88].

In the Lagrangian framework, the trajectory of every particle is calculated separately. This is done by applying Newton's laws ($F = ma$) to ascertain each particle's velocity ($\overrightarrow{u_p}$) and position ($\overrightarrow{x_p}$). Consequently, a series of partial differential equations is resolved for the entire collection of particles as follows [46, 59, 75, 89–91]:

$$\frac{d\overrightarrow{x_p}}{dt} = \overrightarrow{u_p} \tag{9}$$

$$\begin{aligned} m_p \frac{d\overrightarrow{u_p}}{dt} = & \underbrace{\overrightarrow{F_{Gravity}} + \overrightarrow{F_{Buoyancy}} + \overrightarrow{F_{Virtual\ mass}}}_{Body\ force} + \overrightarrow{F_{Brownian}} \\ & + \underbrace{\overrightarrow{F_{Drag}} + \overrightarrow{F_{Pressure\ gradient}} + \overrightarrow{F_{Basset}} + \overrightarrow{F_{Saffmanlift}}}_{Surface force} \\ & + \underbrace{\overrightarrow{F_{Particle-wall}} + \overrightarrow{F_{Particle-Particle}}}_{Contact\ and\ non-contact\ DEM\ related\ body\ and\ surface\ force} \end{aligned} \tag{10}$$

The equation can become quite intricate when it encompasses factors such as two-way coupling, non-spherical particle dynamics, collisional interactions, aggregation processes, and size alterations resulting from condensation and evaporation phenomena. These elements introduce a high level of complexity due to the interdependent and variable nature of the physical processes involved. The equations for the aforementioned forces are specified below:

$$F_{Gravity} = m_p g \tag{11}$$

$$F_{Buoyancy} = m_f g \tag{12}$$

$$F_{Virtual\ mass} = \frac{m_f}{2}\left(\frac{Du_f}{Dt} - \frac{du_p}{dt}\right) \tag{13}$$

$$\begin{cases} F_{Brownian} = \zeta_i \sqrt{\frac{1}{\widetilde{D}} \frac{2k_B^2 T^2}{\Delta t}} \\ \widetilde{D} = \frac{k_B T C_c}{3\pi \mu_f d_p} \end{cases} \tag{14}$$

$$\begin{cases} F_{Drag} = \frac{18\mu_f C_D Re_p}{24\rho_p d_p^2} m_p(u_f - u_p) \\ Re_p = \frac{\rho_f d_p |u_f - u_p|}{\mu_f} \\ C_d = \begin{cases} \frac{24(1+0.15Re^{0.687})}{Re} Re \le 1000 \\ 0.44Re > 1000 \end{cases} Spherical\ particle \\ \begin{cases} \frac{C_d}{k_2} = \frac{24}{Re_p k_1 k_2}\left\{1 + 0.1118(Rek_1k_2)^{0.6567}\right\} + \frac{0.4305}{1+\frac{3305}{Rek_1k_2}} \\ k_1^{-1} = 0.33 + 0.67\varnothing^{-0.5} \\ \log k_2 = 1.8148(-\log\varnothing)^{0.5743} \end{cases} Aspherical\ particle(Gansermodel) \end{cases} \tag{15}$$

$$F_{Pressuregradient} = m_f(\frac{Du_f}{Dt}) \tag{16}$$

$$F_{Basset} = \frac{3}{2} d_p^2 (\pi \rho_f u_f)^{\frac{1}{2}} \int_{t_0}^{t} \frac{\frac{d}{dt'}(u_f - u_p)}{(t - t')^{\frac{1}{2}}} dt' \tag{17}$$

$$F_{Saffmanlift} = \frac{2kv^{0.5}\rho d_{ij}}{\rho_p d_p (d_{lk} d_{kl})^{\frac{1}{4}}} (u_f - u_p) \tag{18}$$

In this context, d_p, m_p and ρ_p represent the diameter, mass, and density of the particle, respectively. Similarly, μ_f and ρ_f denote the dynamic viscosity and density of the fluid. The term u_f refers to the velocity of the fluid at the location of the particle and m_f signifies the mass of the fluid that has been displaced by the particle. In the equation describing Brownian force, ζ_i represents a variable with a zero-mean derived from a Gaussian probability density function. The symbol T stands for the absolute temperature, while $\widetilde{D}$ denotes the Brownian diffusion coefficient. The constant $k_B = 1.3806488 * 10^{-23} \frac{m^2 kg}{s^2 K}$ refers to the Boltzmann constant, and Δt is the time step used for integrating the particle's equation of motion. In the Ganser model for the drag equation concerning aspherical particles, k_1 is identified as the Stokes' shape factor, k_2 is the Newton's shape factor, and $\varnothing$ represents the sphericity of the particle. In the context of Saffman's lift force, k is set at a constant coefficient value of 2.594, and the term d_{ij} represents the deformation tensor.

In pulmonary drug delivery, dimensionless parameters such as Stokes, Reynolds, and Froude numbers are critical. The Stokes number, widely used to describe aerosol dynamics, represents the ratio of a particle's response time to the flow time scale. Particles with high Stokes numbers are inertia-dominated and deviate from streamlines, while those with low values closely follow the fluid flow. The Stokes number is defined as follows:

$$St_i = \frac{\rho_p d_p^2 U_i}{18\mu D_i} = \frac{\tau_p}{\tau_F} \begin{cases} Inertial\ Impaction\ St_i > 1 \\ Gravitational\ sedimentation 0.1 < St_i < 1 \\ Brownian\ motion\ St_i < 0.1 \end{cases} \tag{19}$$

where, U_i is the mean velocity in region i, D_i is the equivalent diameter in region i, τ_p is the particle's characteristic response time, often represented by the relaxation time and τ_F is the fluid's characteristic response time. Increasing particle size and flow rate elevates the Stokes number, which quantifies particle responsiveness to system variations. Higher Stokes numbers indicate greater inertia, causing particles to resist flow redirection and deposit predominantly in the upper airway generations via inertial impaction. DE and DF were plotted against the impaction parameter and Stokes number to illustrate this behavior [60]. DE increases consistently with the Stokes number, affirming its expected behavior. At low Stokes values, particles follow airflow, resulting in minimal deposition. As the Stokes number rises—especially during rapid flow deceleration—particles deviate from streamlines, and inertial impaction predominates. This effect is especially significant in areas with pronounced directional changes, like the left and right upper lobes. Elevated flow rates and particle sizes further increase the Stokes number, reducing particle entry into these regions [92]. Feng et al. observed that larger COVID-19 cough droplets maintained higher velocity and concentration than smaller ones. This is attributed to their higher Stokes number, which reduces the influence of viscous dissipation and enables better momentum retention. In contrast, smaller droplets, with greater surface area-to-volume ratios, lose momentum rapidly due to drag and viscous effects [93]. Nicolaou et al. examined aerosol deposition by analyzing inertial and gravitational influences through the Stokes and Froude numbers. The Froude number, defined as the Stokes number divided by the ratio of gravitational settling velocity to fluid velocity, quantifies the relative dominance of inertial *versus* gravitational forces. In certain airflow regions, the instantaneous

Froude number was up to 3–4 orders of magnitude lower than its reference value, indicating significant sedimentation and underestimation of gravitational effects. Sedimentation dominated particle deposition in the extra-thoracic airways, particularly the mouth. Particles with high Stokes numbers deposited primarily via impaction in the larynx and trachea. Additionally, bifurcation angle variations influenced deposition patterns, with impaction prevailing on the cardinal ridge and sedimentation occurring along inclined airway walls [53].

Atmospheric and therapeutic particles from various sources exhibit a complex, polydisperse size distribution. Conventional *in vitro* methods struggle to capture deposition behavior across sizes, but *in silico* models have improved understanding. In a seminal study, Islam et al. used a large-scale lung model and Rosin–Rammler diameter distribution to evaluate polydisperse aerosols. Their results showed increased DE in the right lung, with larger particles ($d_p > 5$ µm) depositing near upper airway bifurcations, and smaller particles ($d_p < 5$ µm) accumulating along bifurcation walls [58]. Ahookhosh et al. examined aerosol deposition and powder characterization using *in vitro* data. Their results showed that increased inhalation flow rate elevated particle deposition due to enhanced inertia and turbulence. Deposition intensified in the extra-thoracic region, trachea, and tracheobronchial tree, primarily via inertial impaction driven by higher inertial forces [60]. Chalvatzaki et al. investigated the impact of breath holding and mouthpiece diameter on powder deposition. Larger aerodynamic diameters increased deposition in the extra-thoracic region, while particles between 2–4 µm showed higher deposition in the tracheobronchial and alveolar-interstitial regions. In the extra-thoracic area, deposition rose as mouthpiece diameter decreased, though this effect was negligible for particles < 1 µm in deeper lung regions. For larger particles, greater mouthpiece diameter enhanced deposition [67].

Boundary and Initial Conditions

Boundary conditions (B.C.s) define fluid behavior at the boundaries of the computational domain and are essential for solving governing equations in CFD. In pulmonary simulations, B.C.s enable accurate modeling of complex airflow and aerosol deposition, typically applied at respiratory tract inlets, outlets, and airway walls. Accurate pulmonary simulations require physiologically representative boundary conditions. Due to computational constraints, simplifications are often applied, though they must preserve core airflow physics. During inhalation, diaphragm and intercostal muscle contraction lowers thoracic pressure relative to ambient air, driving flow via a pressure gradient between alveoli and the mouth. Most studies apply pressure or flow rate/velocity as inlet conditions for incompressible air. When it came to flow rate/velocity, several methods were used, including constant peak inspiratory flow rate [15, 48, 52, 56, 57] (typically 15, 30, and 60 l/min associated with sedentary, light, and heavy breathing), velocity as a function of inlet radius [26] (parabolic inlet velocity, $u(r) = u_{max}(1 - \frac{r^2}{R^2})$), time-varying sinusoidal parabolic velocity profile [29], and realistic inhalation maneuvers as a function of time [15, 17, 19, 69]. Flow rate critically affects powder deposition by enhancing turbulence and inertial impaction in the ET zone. Airflow velocity over time is typically modeled using idealized sinusoidal functions [21, 42] (Fig. 5-a) or realistic breathing waveforms [17, 31, 94] (Fig. 5-b) simulating DPI and nebulizer inhalation. These waveforms vary with age, health, peak flow, tidal volume, and anthropometric factors. In some cases, particle injection coincides with peak flow rate [10]. Equations (20–22) can be employed to compute the realistic breathing pattern:

$$Q(t) = PIFR.\sin\left(\frac{\pi}{2}\frac{t}{t_{max}}\right) 0 < t < t_{max} \tag{20}$$

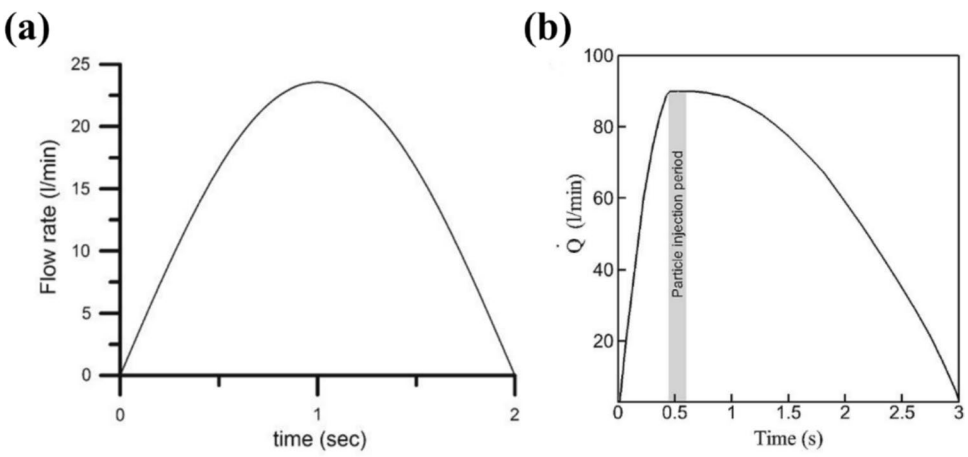

Fig. 5 Flow rate through the mouth as a function of inspiration time: a) idealized sinusoidal functions, and b) realistic breathing waveform profiles of the DPI maneuver (reprinted from Elcner et al. [42] and Bhardwaj et al. [10], with permission from Elsevier).

$$Q(t) = PIFR t_{max} < t < 0.6s \quad (21)$$

$$Q(t) = PIFR.\cos\left(\frac{\pi}{2}\frac{t-(t_{max}+0.15)}{t_{tot}-(t_{max}+0.15)}\right) 0.6 < t < t_{tot} \quad (22)$$

where $Q(t)$ is the flow rate as a function of time, $PIFR$ and t_{max} are the peak flow rate and time to achieve peak flow rate, usually 0.45s, and to get the tidal volume ($\int_{t=0}^{t=t_{tot}} Q(t)dt$), one must determine the value of t_{tot}.

Geometric models in CFD studies often truncate at specific airway generations, limiting accurate representation of terminal airflow pressures and velocities [95]. Consequently, many investigations adopt simplifying assumptions, frequently applying uniform (zero gauge) pressure as the outflow boundary condition. Recent findings indicate that endpoint modeling markedly influences predictions of airflow and particle deposition in upper lung regions [96, 97]. The respiratory tract is lined with a viscous mucosal barrier atop the ciliated epithelium, serving as a primary filtration mechanism for inhaled particles [26]. Mucus thickness varies regionally—from approximately 8.3 µm in the trachea to 1.8 µm in distal bronchioles [98]. Rapidly absorbable medications must traverse this barrier to reach the epithelial surface. Accordingly, the initial deposition site significantly influences absorption patterns, emphasizing the importance of wall boundary conditions in pulmonary drug delivery [99, 100]. Wall boundary conditions—whether rigid or compliant—strongly influence simulation outcomes. Assuming inflexible walls can omit key fluid–structure dynamics, especially in the pulmonary system where lung tissue exhibits viscoelasticity. Incorporating compliant wall conditions with appropriate viscoelastic properties enhances simulation fidelity, improving predictions of airflow and particle trajectories. Pulmonary CFD studies commonly apply immobilized (trapped) boundary conditions for particle deposition, coupled with no-slip conditions for airflow. Deposition is assumed when a particle's center lies within one radius of the wall, while wall-adjacent airflow velocity is set to zero. Reflection and re-suspension are typically neglected due to the mucosal lining of the respiratory tract, which ensures particle adhesion upon impact [136, 173]. Conversely, in the context of particle dynamics against a moistened wall, entrapment upon the surface is contingent upon the particles possessing a velocity inferior to the critical collision velocity, according to the following equation [101].

$$u_{cr} = \frac{3\pi\mu d^2}{2m_p}(1+\frac{1}{e})ln(\frac{z}{z_a}) \quad (23)$$

where μ, d, m_p, e, z, and z_a represent the coefficient of liquid viscosity, the radius of the particle, the mass of the particle, the coefficient of restitution, the film thickness of the liquid, and the roughness of the particle surface, respectively. Since the previous study's particle velocity was up to 7 m/s, for instance, it was predicted that the particle would not trap on the human respiratory system's wall [41, 102].

Initial conditions (t = 0) define the flow variables within the computational domain at the simulation's outset and are vital for transient analyses. These typically include velocity, pressure, temperature, and concentration profiles of the drug-laden aerosol at the domain's inlet. Given their influence on deposition within the lung's complex branching architecture, initial particle size distribution is especially critical. Environmental parameters—such as airflow temperature and relative humidity—should also inform these specifications. Airway wall temperature is typically assumed to match core body temperature (~ 37 °C), while relative humidity near the wall often exceeds 99% [103, 104]. Idealized humidity assumptions may misrepresent droplet size evolution and deposition behavior. Accurate boundary conditions therefore require incorporation of heat transfer physics. Particle injection is generally randomized and uniformly distributed, with initial velocity matching the carrier gas [56].

Effect of Lung Geometry on CFD Modelling

Comparing Traditional 1D and Modern 3D Approaches

In silico methods include semi-empirical whole-lung 1D models—historically the earliest approaches—and increasingly prevalent 3D CFD simulations [16]. 1D models apply algebraic deposition formulas based on either a single airway path or stochastic lung geometry [105]. These are fitted to empirical data using mechanisms such as sedimentation, impaction, and diffusion [16, 106].

1D models offer ease of use, fast results, and accessibility for non-experts, operating efficiently on standard processors. Though initially developed for environmental aerosols, they lack adaptation for therapeutic aerosol transport [66]. They provide sufficiently accurate deposition estimates in distal airways, where aerosol dynamics lessen beyond the trachea [13]. Despite their simplicity, 1D models overlook detailed airway geometry and complex flow dynamics, limiting their ability to predict site-specific particle deposition [37]. They also neglect hygroscopic and evaporative effects, inhaler spray momentum, and anatomical variability across age, sex, and disease conditions [66, 107, 108]. Notable 1D whole-lung models include trumpet, single-path, multiple-path, and stochastic variants. Stochastic models account for the inherent randomness in particle transport and deposition [109]. Originating from Koblinger and Hofmann's 1980s work, the stochastic multiple-path model employed a Monte Carlo approach and probability distributions to capture the asymmetry and variability of the respiratory system. This early work significantly advanced lung particle simulation

via stochastic methods. It introduced a statistical model with randomly selected airway branches and transport paths, allowing size variability. Inhaled particles traverse a stochastic airway network, with each particle following a randomly chosen sequence until deposition occurs [110–113]. The generation of each pathway is stochastic: at every bifurcation, one branch is randomly chosen for continuation, while the other terminates, resulting in particle deposition within the airways. Longest and colleagues have conducted a series of studies on developing a stochastic individual pathway (SIP) model. The method constructs distinct, continuous pathways extending past the third bifurcation into all lung lobes, reaching terminal bronchioles. At each bifurcation, one branch continues while the other ends. A sufficient number of such randomly generated pathways are simulated until deposition data converge to a stable average [16, 21, 36].

To ensure targeted aerosol deposition in the lungs, CFD aerosol models offer advantages over 1D methods by numerically solving transport equations for airflow and particles. CFD can directly account for breathing dynamics, aerosol properties (especially hygroscopic size changes), fluid–wall interactions, and wall motion within complex geometries—whether realistic or idealized [46, 99]. We limit this review to three-dimensional CFD studies due to their advantages. Rising air pollution and respiratory ailments pose a severe risk to human health. As a result, predicting the deposition patterns of harmful and therapeutic inhaled particles is becoming increasingly important.

The Respiratory System: Structure and Function in Drug Delivery

Inhalation offers superior medication absorption compared to injection or oral routes due to the lung's compact epithelial cells and extensive absorption surface [41]. Consequently, understanding airway geometry is essential. Air travels through conducting airways to the bubble-shaped air sacs called alveoli, where gas exchange occurs [52]. Precise comprehension of this pathway is fundamental for optimizing inhaled therapeutics. During inhalation, the diaphragm and respiratory muscles contract, creating negative pressure that draws air into the lungs. During exhalation, these muscles relax, creating positive pressure that expels air [8]. The respiratory system involves the central nervous system, chest wall, pulmonary circulation, and respiratory tract [114]. The human lungs, are conical and divided into right and left sections. The right lung has three lobes, while the left has two lobes to accommodate the heart [26]. The respiratory tract has three sections, each with an iterative branching system spanning 23 generations (Fig. 6).

According to International Commission on Radiological Protection (ICRP) guidelines, a respiratory tract model should include the extra-thoracic (ET; nasal cavity, oral cavity, pharynx, larynx to tracheal entrance), tracheobronchial (TB; trachea to terminal bronchioles, generation 16), and alveolar regions (generations 17–23) [115, 116]. The respiratory tract is commonly classified into upper and lower

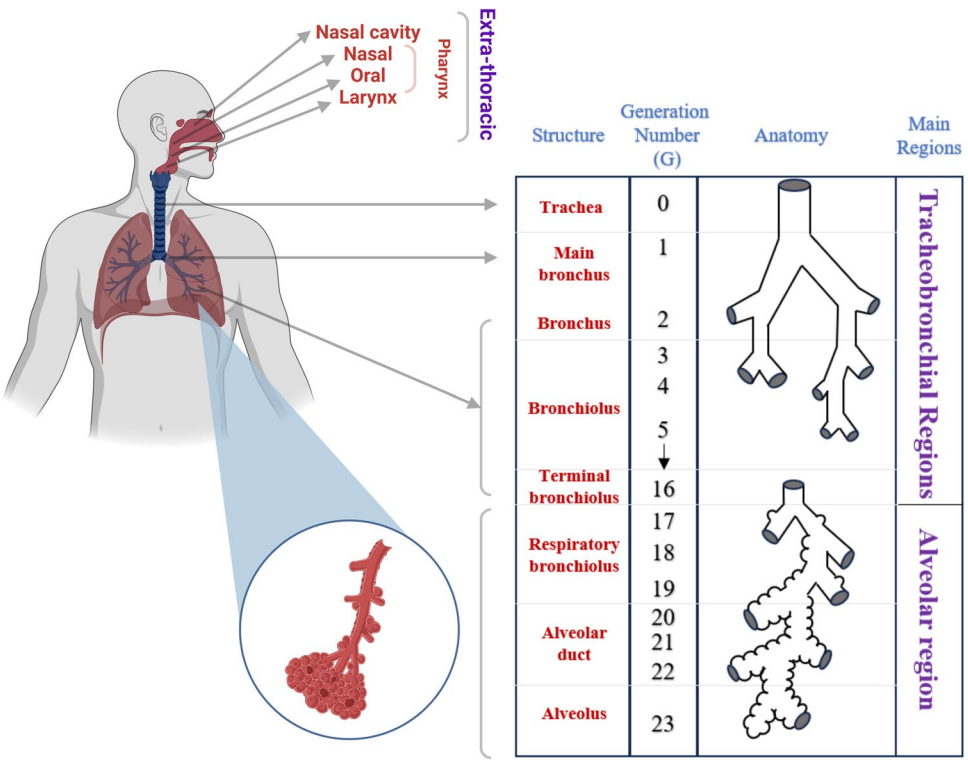

Fig. 6 The diagram displays the branching structure of the adult human airway, which is divided into the extra-thoracic region, tracheobronchial region (G0-G16), and the alveolar region (G17-G23).

regions. The upper tract, akin to the extra-thoracic area, includes all structures above the glottis—namely the oral and nasal cavities, pharynx, and larynx. Numerical results show that inertial impaction significantly influences particle deposition in this region [26]. The lower tract spans from the vocal cords through the intra-thoracic zone, beginning at the trachea and terminating in the alveolar sacs deep within the lungs [117]. Upper airway morphology has a considerable impact on local airflow patterns, as well as particle transport and deposition in the tracheobronchial region. Furthermore, it was discovered that the jet core length remains constant despite higher inhalation flow rates in upper airways [118]. The extra-thoracic (ET) region, referred to as the upper respiratory tract, consists of the oral cavity, nasal cavity, pharynx, and larynx [22]. The anatomical location of the tube-like pharynx (throat), with a mean length of 12.5 cm, divides it into three sections: the oropharynx, which is behind the mouth; the nasopharynx, which is behind the nasal chambers; and the laryngopharynx, which is behind the larynx. The epiglottis is included in the structure of the larynx as well. Warming, humidifying, filtering, and directing air toward the lower respiratory airway passages are the functions of the naso-oropharynx [52]. Incorporating the laryngeal jet is essential for accurate airflow and aerosol deposition predictions in the middle airways due to downstream turbulence generation [118]. Numerical studies identify glottis constriction as the key morphological factor influencing particle transport. Upper airway features—including mouth-to-throat curvature, cross-sectional circularity, pharynx–trachea joining angle, and constriction ratios across the glottis and mouth inlet—affect airflow dynamics, pressure drop, and deposition to varying degrees [119].

Other geometric factors exert relatively minor influence. Enhancing *in vivo* deposition prediction requires understanding pharmaceutical aerosol deposition mechanisms in the mouth–throat (MT) via *in vitro* methods. The USP throat—featuring a uniform circular cross-section and 90° bend—is widely used in CFD simulations and *in vitro* testing [120]. However, USP models, including those applied in stationary tests like the Next Generation Impactor (NGI), lack essential anatomical features of the ET region [121]. The TB region—also termed the conducting zone (generations 0–16)—transports inhaled air to the alveolar gas exchange sites. Its airway structure resembles a branching tree, beginning with the trachea (10–14 cm long, 1.3–2.7 cm in diameter) [122], which bifurcates into right and left main bronchi and further divides into segmental bronchi [20]. This pattern persists dichotomously, where each airway bifurcates into two'child'branches with an approximate diameter of 1 mm at the 16th generation [123]. These branches are identified as generations and sequentially numbered from the top to the bottom. The human lung's largest portion, known as the alveolar region, deep lung region, or acinar region, is contiguous with the terminal segment of the TB region, encompassing all lung components housing alveoli. As we venture further into the lung, the number of alveoli on each generation of respiratory bronchioles progressively increases until the alveolar ducts are entirely encased in alveoli [124]. The tiny tubes that link the alveolar sacs—which include an atrium and many alveoli—to the respiratory bronchioles are known as alveolar ducts. One may roughly represent each sac (alveolus) as a spherically shaped cup [125]. The last seven generations (G17–G23) are often referred to as the alveolar region, while generations 20–23 are referred to as the respiratory zone [126]. This is where gas exchange occurs and is encircled by a network of blood capillaries fed by the pulmonary artery [127]. Limited understanding of flow dynamics and particle deposition in the alveolar region stems from its complex geometry and wall motion [128]. Kolanjiyil et al. [129] developed a physiologically inspired acinar model incorporating breathing-induced wall deformation and partially spheroidal air sacs. Their results showed increased deposition rates with larger particle diameters and higher inhalation tidal volumes.

Challenges of Idealized vs. Realistic Models in Lung Geometry Modeling

Variations in human respiratory geometry significantly influence airflow, aerosol dynamics, and deposition. Lung models are typically classified as idealized or realistic. Idealized geometries simplify anatomical features to facilitate analysis of lung mechanics, while realistic geometries replicate complex, irregular structures for greater physiological accuracy. A major challenge in airway modeling is reconstructing anatomically faithful geometries for reliable flow simulations. To address this, recent efforts have focused on developing refined idealized airway models.

Weibel's model (1963) is one of the most widely adopted geometric frameworks for the respiratory system [126]. It represents a healthy adult lung with a total volume of ~ 4800 ml, of which 66% comprises alveoli. This landmark model laid the groundwork for developing idealized airway geometries and has informed a broad spectrum of experimental and computational studies leveraging its dimensional data [47, 59, 95, 130]. Weibel's Model A is a basic model with a symmetric tree structure. It posits that airways exhibit cylindrical geometry, and each bronchus symmetrically bifurcates into two other bronchial tubes through a regular dichotomy. This implies that the branching elements maintain consistent diameter, length, and angle with their parent, resulting in 2^n elements in the n-th generation [126]. In Weibel's Model A, airway divisions span G0–G16 for the tracheobronchial region, G17–G19 for respiratory bronchioles, and G20–G23 for alveolar ducts. All ducts and sacs in the respiratory zone are fully alveolated,

with each alveolus geometrically represented as a spherical segment [131]. Naturally occurring irregular dichotomy introduces variability in element dimensions and branching angles within the same generation.

To better reflect anatomical variability, Weibel proposed the "B" model to account for irregularities in lung structure. While the "A" model remains widely adopted, the "B" model has seen limited use despite its enhanced realism. Horsfield et al. (1971) later advanced asymmetrical modeling approaches, contributing to more anatomically representative frameworks [132]. This model prompted extensive research into asymmetry's effects on aerosol deposition. While it specifies lengths, diameters, and branching angles for coplanar parent–daughter branches, real lung geometry varies notably across generations [42]. Similar to Weibel's "B" model, it remains underutilized in scholarly studies [8]. Yet, the previously described simplistic models cannot predict the honest particle deposition patterns due to the complexity of the respiratory airway structure, which significantly influences particle deposition.

For *in vitro* and *in silico* studies of airway dynamics, subject-specific realistic airway models are now favored over simplified idealized geometries. These models aim to accurately capture the complex anatomical features of the respiratory system, enabled by advances in medical imaging—particularly computed tomography (CT) scans. Magnetic resonance imaging (MRI), optical coherence tomography (OCT), electrical impedance tomography (EIT), positron emission tomography (PET), and lung ultrasound (LUS) are among the other biomedical imaging modalities used [133, 134]. By using an image registration approach, these imaging modalities are digitally rebuilt. Airflow and particle transport towards the lower airways have been the subject of very few published investigations. The lack of high-resolution CT scans and the high cost of computing have prevented researchers from thoroughly investigating aerosol deposition in this area. Therefore, using suitable mathematical models for the distal airways could be feasible [135, 136]. Figure 7 demonstrates three phases involved in reconstructing the human respiratory airway [52, 59, 137, 138]:

- **Image Acquisition**: CT or MR imaging is used to obtain radiological cross-sectional images of the anatomical region. These images are saved in DICOM format, the standard file format for radiology images.
- **Image Segmentation**: This stage involves extracting regions to isolate specific anatomical structures, such as the airway. The airway is the Region of Interest (ROI) and it is separated from surrounding areas like bones or soft tissue.
- **3D Regeneration and Refinement**: The extracted airway region is exported into Standard Tessellation Language (STL) format files, which are then adjusted to enhance the smoothness of the connections and interfaces. The processed model can be prepared for manufacturing casts for *in vitro* studies or mesh generation for CFD simulation.

Beyond One-size-fits-all: Role of Anatomical Variations in CFD Modelling

The effects of geometric variability on airflow dynamics and aerosol deposition underscore the need for anatomically realistic models. Patient-specific factors—such as gender, age,

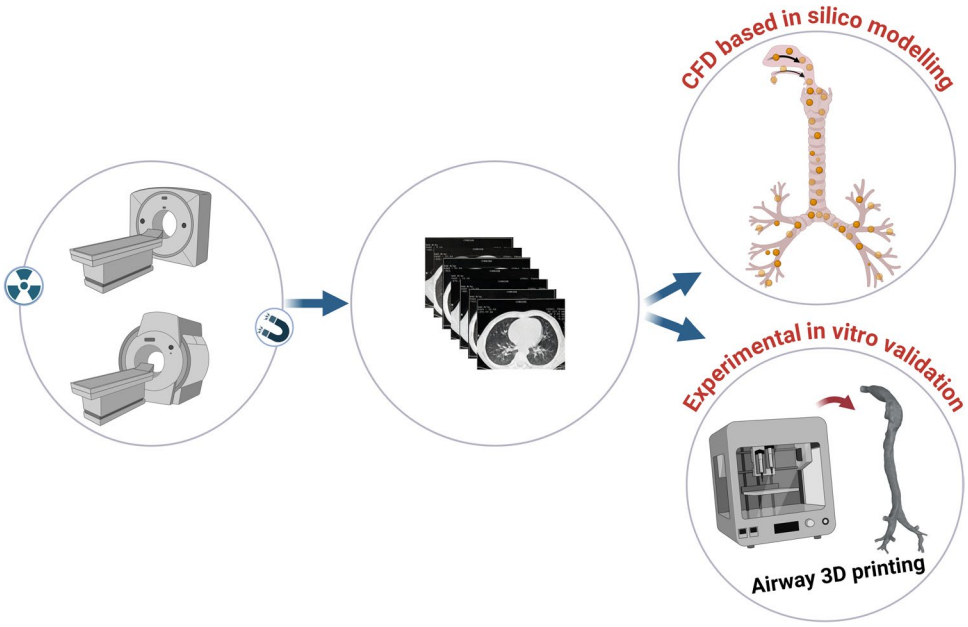

Fig. 7 The reconstruction of the human respiratory airway.

height, weight, and respiratory disorders—can be incorporated into deposition models. However, most current models rely on data from healthy individuals, limiting their applicability for generalizing drug delivery outcomes [124]. CFD modeling is useful in assessing airway obstructions, which reduce airflow and limit aerosol deposition during inhalation therapy due to narrowing from mucus or inflammation [100]. Conditions like cystic fibrosis, asthma, COPD, and pulmonary hypertension cause high local velocities and adverse pressure drops, leading to flow separation and increased impaction losses at deposition hotspots [139]. In patients using DPIs, worsening disease severity and stenosis reduce drug inhalation time and peak inspiratory flow rate [140]. Lower flow rates hinder de-agglomeration, leading to suboptimal drug release and larger particle deposition in the upper airway.

Furthermore, tracheal stenosis impairs breathing and damages the trachea [141]. Bhardwaj et al. [10] optimized inhalation therapy by analyzing glottal motion effects on aerosol deposition via a time-varying parabolic velocity profile. Three glottal expansion ratios—from static to 40% cross-sectional growth—were tested. Dynamic glottal motion notably enhanced airflow and particle deposition during DPI use, with static glottis underpredicting deposition for smaller particles. Larger particles (5–10 µm) show reduced tracheobronchial deposition with a static glottis compared to dynamic glottal motion [10]. Kadota et al. [31] analyzed particle deposition in three COPD patients with varying severity, revealing distinct deposition patterns and distributions. Smaller particles, capable of reaching deeper lung regions, are preferred. These findings support tailored DPI and powder formulations for COPD patients across severity levels.

Internal organs grow proportionally from infancy to adulthood, notably affecting lung capacity, alveolar size, and lung dimensions. These anatomical changes alter respiratory frequency [142, 143]. Understanding particle deposition requires considering age-dependent lung characteristics in children and adults [144]. Children experience higher MT deposition losses due to narrower extra-thoracic airways and lower inspiratory flow rates. Limited pediatric imaging data has constrained *in silico* age-dependent studies to theoretical models [145]. Conversely, aging reduces lung volume and respiratory capacity [146]. Airway diameter and breathing patterns strongly influence deposition, yet are underexplored in younger populations. Das et al. [23] used age-specific inhalation maneuvers to improve aerosol distribution across ages 5 to adulthood. DPI simulations showed peak conducting airway deposition (~ 80%) at a Stokes number of ~ 0.06, while nebulizers reached ~ 45% within 0.03–0.04. These optima highlight the need to reassess inhalation treatment design for children. Islam et al. [4] analyzed polydisperse aerosol transport in individuals aged 50–70. Reduced airway size and flow rate increased deposition efficiency, with larger particles depositing more in the mouth-throat region. Airway dimensions and flow rates strongly influenced flow fields, and older lungs exhibited greater pressure drops than younger ones. Singh et al. [40] investigated aerosol deposition and transport in stenotic airways using three models: a healthy lung and two with left and right stenosis. Their findings, consistent with prior studies, showed that stenotic airways generate complex velocity fields based on numerical results. Airflow velocity is higher in stenotic regions than in healthy airways, and both particle size and flow rate enhance DE. Pressure peaks in the mouth-throat region, while stenotic areas show lower pressure. Overall, deposition fraction is greater in stenotic airways [40].

While most studies focus on lung generations up to G5, Rahman et al. [147] examined aging effects on particle deposition and airflow from G0 to G14. With airway width and breathing capacity declining ~ 10% per decade after age 50, their study assessed particle TD in adults aged 50–70. Nearly all 20 µm particles deposited in upper airways (G0–G5), with none reaching G7. Smaller particles penetrate deeper airways; at 5 µm, over 48% reach beyond G14 into the lower respiratory tract. Aging reduces particle escape through airway generations, resulting in increased upper airway deposition. These findings support age-specific targeting in aerosol drug delivery [45, 148]. Xi et al. [149] investigated the influence of alveolar size on nanoparticle deposition using models containing 1, 4, and 45 alveoli. Their findings reveal that larger alveoli exhibit reduced nanoparticle retention, especially for fine particles (100–800 nm), which are more size-sensitive than ultrafine particles (1–100 nm).

Rahman et al. [46] reported an 83% increase in pressure drop in stenotic models *versus* healthy ones. Higher particle size or flow velocity diminishes the influence of the diffusion mechanism.

Statistical shape modeling (SSM), a computer vision technique, facilitates parametric anatomical model generation. Xi et al. [150] applied SSM to 40 lung models, producing infinite parameterized geometries that capture key morphological features—supporting realistic respiratory analysis and model development. The adjoint method enables efficient sensitivity analysis and aerodynamic optimization. Talaat et al. [151] applied adjoint–CFD modeling to assess airway morphology effects on Acetaldehyde and Benzene deposition, confirming its utility for shape-dependent dosimetry under steady inhalation.

Huang et al. [48] assessed how mouth-throat geometries— US Pharmacopeia throat (USP), idealized mouth-throat (IMT), and realistic mouth-throat (RMT) models—affect small particle deposition. RMT produced more uniform particle dispersion and consistent pharyngeal/laryngeal deposition, with reduced mouth/tracheal deposition. Deposition fraction varies significantly with biological

sex; males typically have larger airway cross-sections during early lung development [152].

Mesh Independence and the Role of Moving Mesh and Viscoelastic Modeling in CFD

When performing the simulations of 3D airway models, a mesh independence test is essential to achieve optimal balance between computational efficiency and accuracy. Mesh independence is established by comparing fluid flow parameters across various grid configurations, such as velocity profiles and regional particle depositions at key cross-sections. For finite volume methods, the 3D model can be meshed using hexahedral, polyhedral, or tetrahedral elements, with prism layers in the near-wall region to capture near-wall boundary layer effects better [34]. Numerical errors, though inevitable, can be minimized through the appropriate refinement of the mesh and the selection of proper numerical schemes. Furthermore, high local mesh resolution is required to obtain accurate estimates of near-wall derivatives, particularly in capturing the boundary layer transitions from laminar to turbulent flow. To accurately resolve the viscous sub-layer, maintaining the first prism layer at a dimensionless wall distance (y^+) below 1 is essential. For example, the shear stress transport (SST) transition model uses the $y+ < 1$ criterion to accurately capture the viscous sub-layer [153]. In this context, $y+$ represents the dimensionless distance from the wall or the local near-wall Reynolds number, as defined in Eq. (24).

$$y^+ = \frac{y}{\upsilon}\sqrt{\frac{\tau_w}{\rho}} \tag{24}$$

where τ_w is the wall shear stress, and y is the absolute distance to the closest wall [154].

During both inhalation and exhalation, the dynamic interactions between lung tissue and airways are correctly represented by the CFD thanks to the moving mesh approach [16]. This approach enables a more precise simulation of airflow and particle movement, essential for investigating inhaled medications'distribution in the lungs. When modeling medication aerosol distribution in the lungs, the moving mesh approach takes into account airway expansion and contraction, as well as lung tissue viscoelasticity [129]. The fluid–structure interaction approach clearly shows the viscoelastic effects of the respiratory tract wall in living tissue. The accuracy of the reaction can be significantly enhanced by using a viscoelastic dynamic mesh, such as the moving deforming mesh [134]. Assessing low Reynolds number flows ($Re < 1$) in the submillimeter human pulmonary acinus is experimentally challenging [155]. Sznitman et al. [128] modeled resting tidal breathing using rhythmic moving-wall boundary conditions. Their results demonstrate that alveolar flow patterns under wall motion differ strikingly from rigid-wall simulations, underscoring the necessity of incorporating inherent wall motion for realistic acinar flow understanding. By extending from generation 10 of the central conducting airways to the pulmonary acinar region, Koullapis et al. aim to forecast deposition during a complete breathing cycle in a simplified approximation of the deep lung. Incorporating a physiologically realistic model of the acinar region sets this study apart from previous efforts. This model enables the simulation of deposition over a complete breathing cycle [29, 66].

To mimic various breathing patterns resulting from negative alveolar pressure, Kolanjiyil et al., introduced a wall-displacement boundary condition at the bottom surface of the first-generation whole-lung-airway model, in their study [47, 156]. In addition, numerous inhalation/exhalation scenarios (rest, exercise, etc.) were implemented by manipulating the wall/mesh displacements to replicate realistic breathing patterns [47]. Exploring the effects of airway deformation on air-particle dynamics, Zhao et al. [5] utilized a disease-specific elastic truncated whole-lung model. The results showed significant differences in air-particle flow estimates between static and elastic lung models, highlighting the critical importance of airway deformation kinematics modeling in whole-lung models. The continuity and Navier–Stokes equations with a moving boundary can be expressed as:

$$\frac{\partial(u - u^{mesh})}{\partial x} = 0, \tag{25}$$

$$\frac{\partial u}{\partial t} + \left(u - u^{mesh}\right)\frac{\partial u}{\partial x} = -\frac{1}{\rho}\frac{\partial p}{\partial x} + \frac{\mu}{\rho}\frac{\partial \tau}{\partial x} + g \tag{26}$$

where u is the fluid velocity, u^{mesh} is the velocity of the moving mesh, and p is the pressure. ρ and μ are the density and viscosity of air, respectively. u^{mesh} can be given by $\frac{\partial x}{\partial t} = 0$, where x is related to the local position of the wall boundary.

Computational Challenges and Cost-saving Strategies

One notable drawback of using CFD in pulmonary drug delivery is the significant computational expense involved. The complex simulation of airflow patterns, particle behavior, and their interaction with complex lung structures demands significant computational resources and lengthy simulation times [16]. There have been efforts in recent years to address this issue. By decomposing the tree according to the flow similarity throughout the central conducting regions during sinusoidal breathing, Koullapis et al. [29] reported a reduction in processing cost. Finally, airflow and particle transport are simulated in one typical bifurcation for a given generation and one representative sub-acinus

unit, resulting in significant computational cost reductions. In an additional investigation, they evaluated regional aerosol deposition influenced by mouth-throat geometry using a cost-effective LES approach at inhalation flow rates of 30 and 60 L/min [57]. Variations in the flow field across three extra-thoracic geometries mostly vanished beyond the major bifurcation. If patient-specific particle escape distributions are known or predictable, regional tracheobronchial deposition can be accurately estimated. These results provide hope for large computational cost savings, particularly in the context of *in silico* population studies, where the precomputed flow field and aerosol size distribution from standardized mouth-throat models can be applied to a large number of tracheobronchial trees found in chest-CT databases, reducing radiation exposure for the patient [57]. Kolanjiyil and colleagues combine 1D and 3D geometries to model the entire lung structure, offering a cost-effective approach for analyzing particle transport [156]. Initially, the respiratory tract geometry is depicted as a 3D configuration from the mouth to the trachea, followed by the consolidation of all succeeding airways into a 1D conduit that expands exponentially [156]. Similar research was done by Kolanjiyil et al., who effectively analyzed aerosol dynamics computationally and compared the results to those of *in vivo* data [47]. The whole-lung airway model configuration includes personalized upper airways from the nose/mouth to approximately generation 3, subsequently linked to adaptable triple bifurcation units (TBUs). Using morphometric data of human lung casts, these TBUs are arranged in series and parallel to cover the remaining generations.

Powder Characteristics: Impact on Flowability and Lung Deposition in Numerical Study

Dry powder inhalers (DPIs) use carrier-based formulations, where fine drug particles are blended with larger lactose carriers (50–200 µm) for uniform distribution and effective delivery [24]. The powder is capsule-loaded and released upon rupture. Proper inhaler mechanics are essential for de-agglomerating particles and ensuring drug detachment for targeted lung delivery [157]. Common dry powder production methods for pulmonary drug delivery include spray drying, spray freeze-drying, milling, and supercritical fluid techniques [158, 159]. These approaches yield powders with optimal particle size, shape, and properties for efficient lung-targeted inhalation therapy. Various physicochemical properties of medications and excipients play a crucial role in determining the characteristics of a formulation. It is essential to strike a balance between the removal forces during inhalation and the adhesion forces between the drugs and carrier particles to guarantee efficient distribution of small drug particles [86, 160].

Metrics for Quantitation Aerosol Drug Delivery Performance

Aerosolization performance is evaluated via stationary testing using key metrics: mass median aerodynamic diameter (MMAD)—the diameter at which 50% of particle mass lies above and below; fine particle fraction (FPF)—the proportion of particles < 5.0 µm; and emitted dose (ED)—the amount of drug exiting the device and reaching the patient's mouth [161]. Testing is conducted under fixed flow rate and volume conditions. It is commonly assumed that a combination of high FPF, high ED, and low MMAD will reduce upper respiratory tract depositional waste and a higher aerosol delivery efficiency to the deep lung. On the other hand, the deposition efficiency (DE) and deposition fraction (DF) may be used to quantify the localized drug particle deposition in the respiratory tract of humans as follows.

$$DE = \frac{The\ quantity\ of\ particles\ deposited\ in\ a\ particular\ region}{The\ quantity\ of\ particles\ entering\ this\ specific\ region} \quad (27)$$

$$DF = \frac{The\ quantity\ of\ particles\ deposited\ in\ a\ particular\ region}{The\ quantity\ of\ particles\ entering\ through\ the\ mouth\ in\ let} \quad (28)$$

Mechanisms of Aerosol Deposition in Respiratory Airways

Numerous factors influence powder characteristics, as illustrated in Fig. 8. Particle interaction with airway walls depends on size and airflow dynamics and is governed by inertial impaction (3–6 µm), gravitational sedimentation (1–3 µm), Brownian diffusion (< 1 µm), and turbulent dispersion [117, 162]. Additional factors such as electrostatic charge, coagulation, and physicochemical properties further impact particle transport and deposition [38]. Upper airway aerosol deposition is primarily governed by impaction, driven by high airflow velocities and abrupt directional changes. Particle inertia causes deviation from streamlines and wall collisions, with larger particles exhibiting greater impaction propensity due to size [53]. In deeper, narrower lung airways, particles tend to deposit via diffusion and sedimentation due to reduced velocities and prolonged residence times. Larger particles primarily settle by sedimentation, while sub-micron particles deposit through Brownian diffusion [115]. At modest flow rates, gravitational sedimentation also becomes prominent in larger airways during targeted drug delivery [163]. Turbulent dispersion also contributes to small particle deposition, as flow irregularities alter particle trajectories [53]. Following deposition, species absorption begins due to concentration gradients between air, tissue, and across tissue layers. Substances dissolve in the mucus

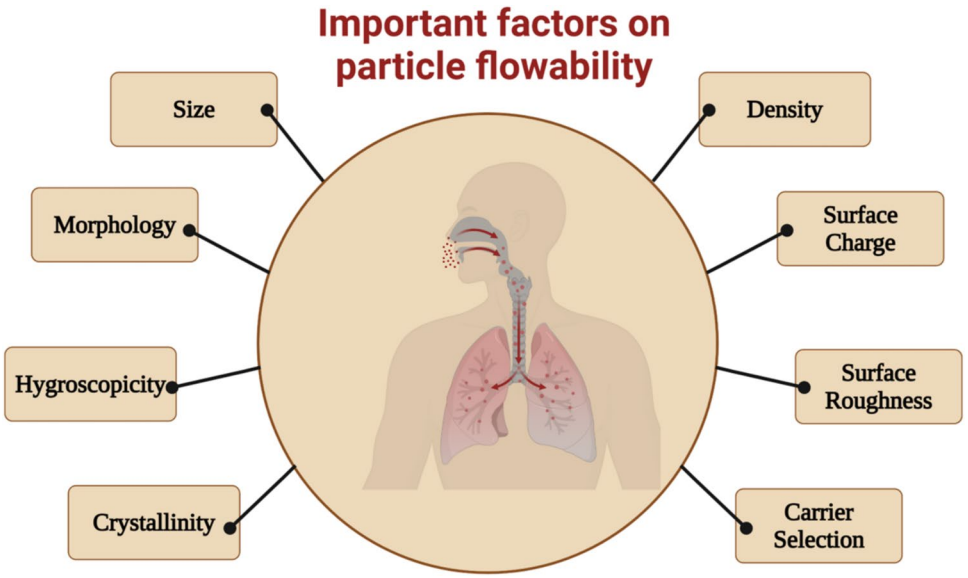

Fig. 8 Key factors influencing particle flowability and resulting lung deposition.

layer, permeate underlying tissues, and are ultimately cleared via the bloodstream [99, 100].

Essential Characteristics of Inhalable Powders for Accurate CFD Modeling

Both pharmaceutical and environmental aerosols exhibit complex size distributions, with particle size being the key determinant of deposition throughout the respiratory tract [58]. Inhaled aerosols typically range from 0.01 to 100 µm and may exist as solid particles or liquid droplets [124]. Effective delivery to deep lung airways via DPIs requires particles with aerodynamic diameters between 1–5 µm. CFD simulations primarily aim to predict the fine particle fraction (FPF) capable of reaching these regions. Since a portion of inhaled particles inevitably deposits outside the target zone, safety and potential adverse effects of inhalation therapy warrant careful consideration [164]. Particle deposition in the respiratory tract varies with aerodynamic size: 20–30 µm in the pharynx, 10–20 µm in the larynx, 8–10 µm in the trachea, 5–8 µm in the bronchial tube, 3–5 µm in the bronchiole, and 0.5–3 µm in the alveoli [165]. Larger particles deliver higher doses but tend to deposit in central airways, whereas smaller particles reach peripheral regions with lower delivered doses [30].

Additionally, aerosol particle size can undergo dynamic changes due to coagulation, condensation, and evaporation. Hygroscopic particles enlarge in response to elevated moisture and relative humidity in the respiratory tract. Water droplets from nebulized aqueous formulations experience rapid evaporation or condensation, altering particle behavior and deposition patterns. Humidity affects lactose-based DPI formulations by smoothing rough particle surfaces and forming solid bridges, especially among amorphous and fine particles [166]. Moisture sorption increases cohesive forces, impeding flow and aerosolization, and promoting larger non-inhalable agglomerates [167]. Additionally, relative humidity significantly alters electrostatic interactions, impacting triboelectric charging and aerosolization efficiency [168]. Furthermore, it appears that the rise in the rise in the upper airway is hygroscopic growth, which results in increased inertial impaction. Compared to hydrophobic particles, hydrophilic particles are more likely to absorb water, reducing the effectiveness of pulmonary administration. Applying modified hydrophobic agents to the surface of particles is a widely recognized and useful tactic [169, 170].

The morphology and porosity of inhaled particles critically affect drug distribution across respiratory regions. Modifying non-spherical shapes enhances penetration, deposition, and functional performance [171]. Morphological discrepancies—particularly between elongation and sphericity—strongly influence deposition patterns of inhaled formulations [95]. Elongated carriers offer a distinct advantage over spherical ones, facilitating drug deposition in the lower airways and achieving higher FPF values. This phenomenon could be attributed to the reduced cross-sectional area of non-spherical particles, leading to lower opposing drag forces as described by Eq. (29) where C_D is the drag coefficient. While an increased elongation ratio (ER) positively impacts pulmonary delivery, there is an optimal point beyond which further increases in ER do not significantly affect the FPF [172].

$$F_D = 0.5\rho u^2 C_D A \tag{29}$$

Ohsaki et al. [41] demonstrated that particle shape significantly influences deep lung deposition. In a simplified respiratory model, rod-shaped particles with higher aspect ratios achieved enhanced penetration due to their longitudinal alignment with high-velocity flow.

Additionally, Tomahawk-shaped particles exhibited superior deposition compared to cylindrical forms, attributed to their unique drag characteristics. Cylindrical drug particles exhibit superior cellular absorption efficiency compared to spherical forms [41, 95]. Amorphous materials—commonly generated via spray drying—enhance the bioavailability of poorly water-soluble drugs and possess lower densities than their crystalline counterparts, facilitating improved formulation flexibility for standalone or combination therapies [173]. Particle density is another key attribute that directly influences the aerosolization behavior of particles. To determine the bulk density (ρ_b) of a powder, a set procedure involves measuring the volume of a known weight of the powder that falls under its weight into a calibrated measuring cylinder. To determine the tapped density (ρ_t) of the same samples, a different method was employed using a tamping volumeter. The volumeter was used to tap the powder repeatedly until no further change in volume was observed, thereby giving the tapped density value. Each density was determined by dividing the mass of the sample by the volume. The following formulas were used to calculate Carr's compressibility index (CI) and Hausner's ratio (HR) [174].

$$CI = \frac{\rho_t - \rho_b}{\rho_t} * 100 \tag{30}$$

$$HR = \frac{\rho_t}{\rho_b} \tag{31}$$

Carr's Index reflects powder flowability, with values < 25% indicating good flow and > 25% suggesting a tendency to agglomerate. Lower Carr's Index values are generally associated with enhanced aerosolization. Similarly, Hausner Ratio (HR) < 1.25 signifies freely flowing powders, whereas HR > 1.25 indicates poor flowability [175, 176]. Particles with tapped densities below 0.4 g/cm^3 are considered beneficial for inhalation therapy [177]. Reduced powder density enhances FPF by extending airborne residence time. Porous, low-density particles consistently demonstrate superior performance in pulmonary drug delivery. Surface roughness markedly affects API (Active Pharmaceutical Ingredient)–carrier adhesion, influencing de-agglomeration and drug interactions via particle surface energies, as shown through atomic force microscopy (AFM) and cascade impactor experiments [178]. Like elongation ratio, surface roughness exhibits an optimal threshold; beyond this, excessive corrugation may hinder rather than enhance performance [179]. In contrast to physiological reality, many of these critical factors are neglected in computational simulations, resulting in significant deviations from corresponding *in vivo* and *in vitro* experimental results.

Validation of Computational Outcomes with Corresponding Experimental Findings *In-vitro* & *In-vivo*

CFD modeling of flow within inhalers and airways is increasingly utilized to analyze fluidization, disaggregation, transport, and deposition processes. When integrated with *in vivo* and *in vitro* experiments, these simulations can guide innovative inhaler design. However, validation remains limited due to diverse modeling approaches and assumptions regarding inhalation dynamics, powder properties, and lung geometry. Even basic models require further adjustments to account for complex phenomena such as evaporation, condensation, agglomeration, and drug–wall interactions—necessitating empirical data for accurate calibration and verification [106, 180, 181]. Clinical approval of new or generic drugs/products requires bioequivalence, either *in vivo* or *in vitro* [182, 183]. Advanced nuclear imaging—such as 2D gamma scintigraphy, single photon emission computed tomography (SPECT), and positron emission tomography (PET)—traces *in vivo* deposition when aerosols are tagged with radioactive markers. These techniques are vital for designing respiratory delivery systems like DPIs, pMDIs, and nebulizers, enabling precise assessment of drug distribution [17, 21, 184]. On the other hand, in pharmacokinetic studies, lung deposition is estimated from drug concentrations in blood and urine samples collected post-administration, offering a non-invasive view of its respiratory distribution [185–187]. Although particle deposition has been studied in human tissues and animal models, ethical concerns and radiation risks significantly limit experimental research. These constraints prioritize patient safety. Moreover, radio-nuclide imaging is complicated by the need for precise drug labeling to preserve aerodynamic properties critical for targeted delivery. Obtaining high-resolution spatial data to quantify particle behavior in human lung airways remains difficult, yet such detail is vital for evaluating links between exposure levels, absorption rates, and health outcomes [28, 38, 188, 189]. Pharmacokinetic approaches offer only rough estimates of total pulmonary deposition, lacking information on precise deposition sites.

In vitro techniques provide precise geometric parameters, allowing systematic investigation of particle size and flow rate effects on pulmonary drug accumulation. This widely adopted method enables direct comparison with numerical simulations using identical geometries. Advances in biomechanical geometry using CT and MRI reconstructions enable highly detailed anatomical models [134]. *In vitro* studies remain standard for assessing particulate deposition in lower airways and validating CFD findings. Historically, airway casts—made by injecting hardening agents into hollow organs like the lungs—were among the first methods to replicate respiratory anatomy [190, 191]. Moreover, 3D printing

of lung models represents a major medical advancement, offering new opportunities for treatment and research. Few teams have explored 3D-printed molds [60]. Unlike *in vitro* benchmarks, validating CFD aerosol forecasts via *in vivo* data remains rare. Lab-made replicas still fall short of the lung's intricate structure and are costly and time-consuming, limiting routine use [124].

Airspeed at the mouth inlet is experimentally assessed using techniques like Laser/phase-Doppler anemometry and Magnetic Resonance Velocimetry (MRV), though measurements are limited to the mouthpiece outlet. CFD is thus employed to model inhaler and lung dynamics. While simulations often assume uniform inlet velocity, realistic profiles improve particle deposition predictions [42, 192–194].

Accurate CFD–*in vivo* agreement relies on precise initial estimates of particle size distribution (PSD), highlighting the synergy between *in vitro* and computational methods. PSD is typically measured across various inhalation flow rates using cascade impactors such as Andersen Cascade Impactor (ACI), the Multistage Liquid Impinger (MLI), the Marple-Miller Impactor (MMI), and the Next Generation Impactor (NGI). These instruments are endorsed by both the United States Pharmacopoeia (USP) and the European Pharmacopoeia (EP) for standardized assessments [195–197]. The descending cut-off diameter at lower stages enables determination of aerodynamic diameter distribution. Impactors operate at a constant flow rate, typically generating a 4 kPa pressure drop across the DPI via vacuum pump. While they don't replicate lung geometry, they yield valuable data on drug characteristics for therapeutic input. However, cascade impactors struggle to assess particle reachability in complex airway structures. NGI-based DPI experiments feature a pre-separation chamber followed by multiple stages for fine particulate collection. To prevent particle rebound, impactor stages are coated with a tween80 ethanolic solution. Drug quantification is typically performed via HPLC analysis [198, 199]. Nebulizer-generated aerosol sizes are measured in chilled NGI setups, allowing rapid particle condensation and staged collection [30]. These tests yield key metrics—FPF, MMAD, and Geometric Standard Deviation (GSD)—crucial for characterizing aerosol size distribution and aerodynamic behavior.

They are determined based on the specific cut-off diameter and the flow rate used during the tests. For instance, the NGI has defined cut-off diameters that are outlined in the Copley report [200], which serve as a standard reference for these measurements according to Table I:

As shown in Fig. 9 from our prior work, velocity magnitude, airflow streamlines, pressure contours, polydisperse particle deposition patterns, and cross-sectional velocity contours were analyzed during a 60 L/min inhalation cycle. The formulation was examined via *in vitro* 3D printing and CFD simulation using realistic airway geometry. The model employed the k-ω SST turbulence model for the continuous phase and Lagrangian-DEM for the discrete phase in ANSYS Fluent.

Table I NGI cut-off Diameter (μm) according to Copley report [200]

	15 L/min	30 L/min	60 L/min	100 L/min
Stage1	14.1	11.72	8.06	6.12
Stage2	8.61	6.4	4.46	3.42
Stage3	5.39	3.99	2.82	2.18
Stage4	3.3	2.3	1.66	1.31
Stage5	2.08	1.36	0.94	0.72
Stage6	1.36	0.83	0.55	0.4
Stage7	0.98	0.54	0.34	0.24

Tables II and III provide a comprehensive overview of contemporary studies in the domain of CFD applied to pulmonary drug delivery systems based on geometry type. They delineate each study according to a set of criteria: particle size, CFD models utilized, flow rates, geometries, computational platforms employed, any associated experimental methodology, and the primary objectives of each research paper.

Challenges and Future Perspectives

Due to its practical applications, the study of airflow patterns and particle transport within the lungs has gained increased attention among biomedical engineering researchers. However, developing precise and effective numerical respiratory tract models remains challenging. This difficulty arises from the complex structure of the airways, the intricate behavior of airflow, and the complexity of aerosol mechanics, all of which require substantial computational resources. Oversimplified assumptions in computational analyses have also led to inaccuracies compared to real biological conditions. A cross-disciplinary foundation is essential for conducting scientifically sound CFD simulations of lung aerosol dynamics.

Few studies have investigated airflow and particle transport in complete lung models under realistic conditions, due to limited CT data and high computational demands. Consequently, most CFPD models focus on segments like the mouth-to-bronchial region or alveoli. Future research should develop more anatomically accurate models—including deeper, asymmetrical pathways—to enhance drug delivery simulations. Precise airway reconstruction and mesh generation remain critical to these efforts. Most lung aerosol simulations use a single airway model and overlook individual variability in airflow and deposition. These models are typically derived from healthy subjects, neglecting anatomical

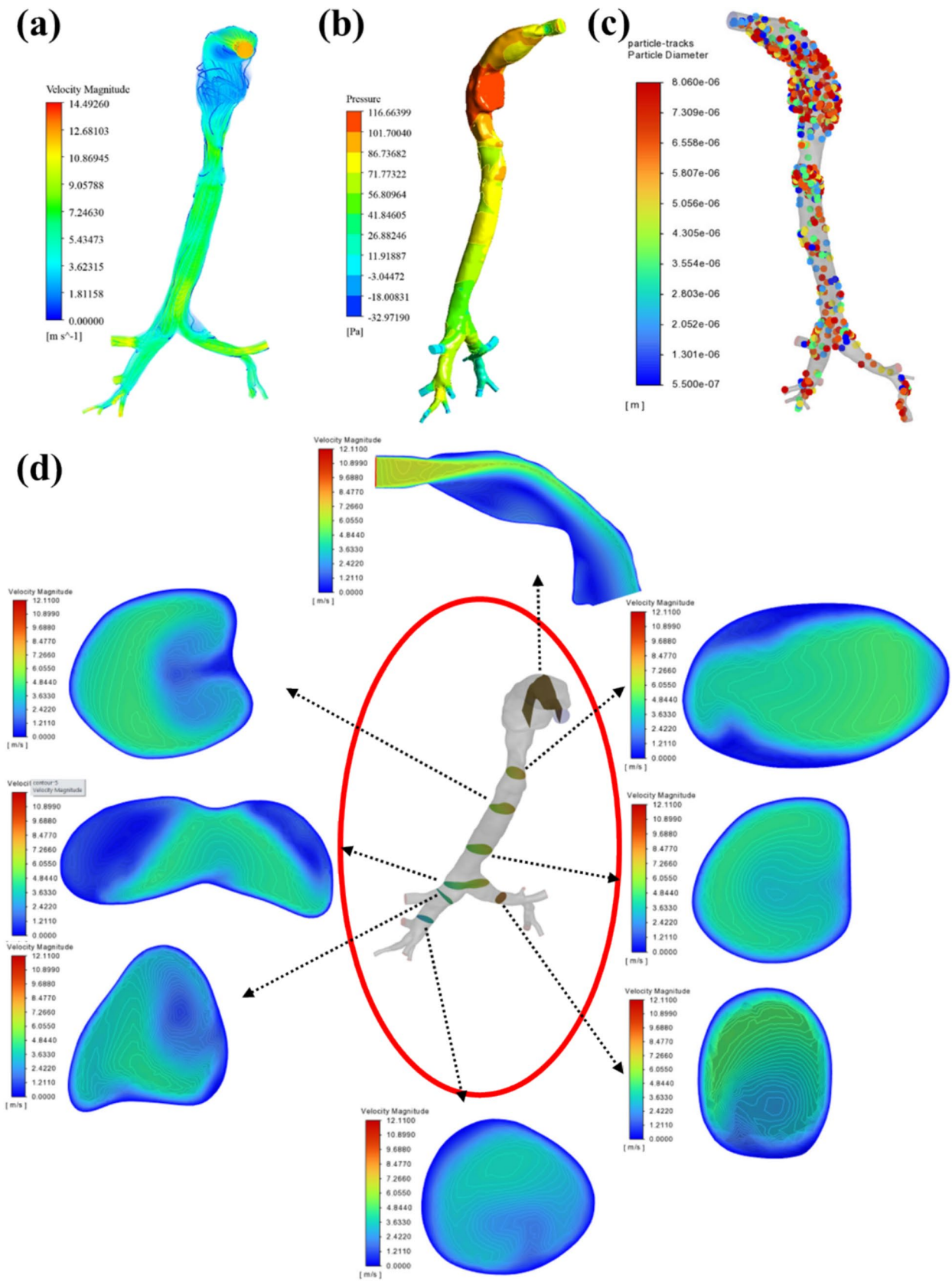

Fig. 9 A visual example of **a**) velocity magnitude with streamlines of airflow, **b**) contours of pressure distribution, **c**) deposition patterns for polydisperse particles, and **d**) contours of velocity magnitude at various cross-sections during an inhalation cycle with a flow rate of 60 L/min [9].

Table II Recent literature on CFD-based research for pulmonary drug delivery systems using idealized geometry

particle size (μm)	CFD model	Flow rate (L/min)	Idealized Geometry	Modeling platform	Experimental method	Main objective	Ref
0.93, 1.79, 2.79, 4.0, 6.07, 9.8, 16, 23.8 and 30	Turbulency (RANS k-ω-SST), Lagrangian (DPM)	15, 30, 45, and 60	3-D mouth-to-trachea and lumped 1-D subsequent airways	ANSYS CFX	Compared to *in vivo* results	Low-cost analyzing particle transport by coupling 3D and 1D geometries with a moving wall method	[156]
0–10	Turbulency (RANS k-ω-SST), Lagrangian (DPM)	PIFR: 54, 65 and 99	3-D mouth-to-trachea and lumped 1-D subsequent airways	ANSYS CFX	*In vitro* NGI and compared to *in vivo* gamma scintigraphy radio-labeled budesonide	Cost-effective particle transport analysis and comparison to experimental data under realistic breathing maneuvers	[17]
3	Laminar and Turbulency (RANS k-ω-SST), Lagrangian (DPM)	15	Whole-lung airway model	ANSYS CFX	Compared to *in vivo* results	Efficient computational analysis of aerosol dynamics using a moving mesh model of the alveoli and compared to *in vivo* data	[19]
2, 3, 5, 6, 8, and 10	Laminar, Lagrangian (DPM)	15	Acinar region	ANSYS CFX	Compared to *in vivo* results	Analyzing aerosol dynamics in a moving acinar region under physiological conditions and comparing to *in vivo* results	[129]
0.1 – 10	Laminar, Lagrangian (DPM)	PIFR: 25.6	Bronchial tree	OpenFOAM	-	Reduced computational cost by utilizing flow similarity during sinusoidal breathing and incorporating a realistic moving mesh model of the acinar region	[29]
0.1–10	Lagrangian (DPM)	time-varying profile	Bifurcating tree coupled to multiple sub-acinus models	OpenFOAM	-	Studying how different breathing profiles, breath-holding, and gravity orientation affect deposition in the deep airways with a moving sub-acinus domain	[66]

Table II (continued)

particle size (μm)	CFD model	Flow rate (L/min)	Idealized Geometry	Modeling platform	Experimental method	Main objective	Ref
2, 2.2, 2.4, and 2.6	laminar and Turbulency (RANS LRN k- ω), Lagrangian	PIFR: 99, 65, and 54	Whole-airway	-	*In vivo* 2D gamma scintigraphy and *in vitro* cascade impaction	Studying aerosol deposition, characterization, and experimental validation with varying inhalation maneuvers using acinar moving wall models	[16]
4 and 10	Turbulency (DNS), Lagrangian (DPM)	15 and 30	Extra-thoracic	-	-	Analyzing aerosol deposition influenced by inertial and gravitational effects using Stokes and Froude numbers	[53]
Spherical and Rod-Like Particles 5–20	Turbulency (RANS standard k-ω), Lagrangian (DEM)	-	Upper airway and bronchial airway	EDEM and ANSYS Fluent	-	Studying how particle–wall interaction and particle shape affect particle deposition in the deep lung	[41]
1–12	Turbulency (RANS k-ω-SST), Lagrangian (DPM)	PIFR: 40, 60, and 90	Age-dependent mouth- throat -trachea-bronchial tree	ANSYS Fluent	-	Optimizing aerosol delivery considering age variations from five years to adulthood with age-appropriate inhalation maneuvers	[23]
5, 10, and 20	Turbulency (RANS Realizable k- ε), Lagrangian (DPM)	60	Age dependent tracheobronchial and Alveolar region	ANSYS Fluent	-	Studying the impact of aging on particle deposition and airflow distribution	[45]
Sphere, Cylinder, and Tomahawk 2.5, 5, and 7.5	Laminar, Lagrangian (DEM)	30	Conducting airway zone	ANSYS Fluent	-	Exploring the deposition of non-spherical drug particles	[95]
1–7	Laminar and Turbulency (RANS LRN k-ω), Lagrangian (DPM)	PIFR: 41.2, 47.1, and 99	Mouth–throat, tracheobronchial tree and alveolar region	-	*In vivo* 2D gamma scintigraphy and *in vitro* NGI and MLI	Studying aerosol deposition, characterizing, and validating using experimental methods for DPI and SMI during actual inhalation maneuvers	[21]
-	Turbulency (LES)	15 and 60	Mouth-throat	OpenFOAM	-	Stable and unstable airflow during light and heavy breathing	[55]

Table II (continued)

particle size (µm)	CFD model	Flow rate (L/min)	Idealized Geometry	Modeling platform	Experimental method	Main objective	Ref
2, 5, and 10	Turbulency (LES), Lagrangian (DPM)	15, 30, and60	Mouth-throat	OpenFOAM	-	Studying 3D vortices and uniform particle spread at different breathing rates	[56]
0.1, 0.2, 0.5, 1.0, 2.0, 5.0, and 10.0	Turbulency (RANS k-ω-SST), Lagrangian (DPM)	atmosphere inlet pressure	Whole-lung model from mouth to alveoli	ANSYS Fluent	-	Investigating the impact of airway deformation on air-particle dynamics in a disease-specific elastic truncated whole-lung model	[5]
0.001–1	laminar	0.3 mm/s	Alveolar region	ANSYS Fluent	-	Assessing how alveolar size influences nanoparticle deposition and the interplay of underlying deposition mechanisms	[149]

PIFR: Peak Inspiratory Flow Rate; NGI: Next Generation Impactor; MLI: Multistage Liquid Impinger; DPM: discrete phase model; DEM: discrete element method

and physiological differences in patients with respiratory conditions. Additionally, studies often exclude inhalation devices, ignoring potential losses of powder in the device or capsule and airflow.

Many studies overlook the viscoelastic behavior of airway walls. Incorporating dynamic meshes that simulate wall motion and deformation can enhance model accuracy, especially in conditions like COPD. Small aerodynamic particles may be exhaled if not effectively deposited, yet exhalation is often excluded from analyses. Breath-hold practices are also frequently omitted. Moreover, most models rely on steady flow rates rather than replicating realistic *in vivo* breathing patterns.

A major limitation of CFPD models is their inability to fully represent complex aerosol physics, including collisions, electrostatic effects, phase changes, and agglomeration dynamics. Many studies simplify by assuming aerosols are non-hygroscopic and uncharged. One-way coupling neglects particle-induced airflow modifications and interparticle interactions. Accurate modeling requires detailed aerosol characterization—such as FPF, MMAD, and density—typically derived from *in vitro* data. Moreover, most aerosols are nonspherical (e.g., fibrous), but CFD models often assume sphericity, reducing accuracy in deposition predictions.

Efficient pulmonary delivery of nanoparticles remains challenging, as nanoparticles that minimally deposit in the lungs may be exhaled. A promising solution uses"Trojan"particles, in which nanoparticles are encapsulated within microparticles [9]. Once in the lungs, the microparticles dissolve, releasing the nanoparticles. This approach combines the favorable aerodynamic properties of microparticles with the clearance-evading characteristics of nanoparticles, enhancing therapeutic delivery and retention in the lungs. This scenario is rarely explored in CFD studies despite its relevance to advanced drug delivery technologies like liposomal dry powder formulations.

Emerging Pharmacokinetic/Toxicokinetic (PBPK/TK) models, when integrated with CFPD models, provide a novel method for predicting the fate of substances after deposition and absorption in the respiratory tract based on mass transfer equations [27, 201–203]. This process can model how particles permeate airway walls, forecast plasma, tissues, and urine concentrations, and predict drug and metabolite accumulation. These models simulate the transport of aerosols to organs through the blood, mucus/tissue diffusion, air-tissue absorption, and convection–diffusion in the airways [78, 196].

AI algorithms analyze medical data—respiratory sounds, CT/MRI images, and clinical records—to detect early lung disease and enhance diagnostic accuracy. In the future, integration of AI with CFD will facilitate personalized lung modeling and targeted drug delivery by optimizing

Table III Recent literature on CFD-based research for pulmonary drug delivery systems using realistic geometry

particle size (μm)	CFD model	Flow rate (L/min)	Realistic Geometry	Modeling platform	Experimental method	Main objective	Ref
1–10	Turbulency (RANS LRN k-ω), Lagrangian (DPM)	30, 60, 90, and 120	Extra-thoracic, trachea, and bronchial airways	ANSYS Fluent	*In vitro* NGI and compare to prototyping 3D printer	Investigating aerosol deposition, characterizing the powder, and validating results with *in vitro* data	[14]
1, 6, 10, and 14	Turbulency (RSM), Lagrangian (DPM)	15, 30 and 60	From the trachea to the end of segmental bronchi	ANSYS Fluent	-	Examining breathing dynamics and aerosol transport while investigating the influence of inertial impaction	[52]
1–12	Turbulency (RANS k-ω-SST), Lagrangian (DPM)	PIFR: 90	Tracheobronchial tree	ANSYS Fluent	-	Examining the impact of glottal motion on aerosol deposition using a time-varying parabolic velocity profile	[10]
-	Turbulency (RANS SST), Lagrangian (DPM)	37 and 75	Realistic CT scan and Idealized (upper airway and tracheobronchial tree)	ANSYS Fluent and ANSYS CFX	Compared to Magnetic Resonance Velocimetry	Subject-variability study of upper airway morphological influence on the airflow regime and comparing the results to Magnetic Resonance Velocimetry data	[49]
1–30	Turbulency (RANS SST), Lagrangian (DPM)	15, 30, 60, and 90	Realistic CT scan, Idealized, and USP (mouth-throat)	ANSYS Fluent	-	Investigating the impact of variations in mouth-throat geometry on fine particle deposition	[48]
1–10	Turbulency (RANS standard k-ω), Lagrangian (DPM)	30 and 60	Mouth–throat and upper airway	ANSYS Fluent	-	Studying the influence of a low-density helium–oxygen mixture on particle transport	[15]
1–10	Turbulency (LES), Lagrangian (DPM)	7.5, 15, 30, and 60	Mouth–throat, upper airway, and bronchial airway	ANSYS Fluent	-	Moving polydisperse aerosols through lung geometries tailored to specific age groups	[4]
1–10	Turbulency (LES), Lagrangian (DPM)	9, 25, and 60	17-generation anatomical model	ANSYS Fluent	-	The large-scale lung model's interaction with aerosols of different sizes	[58]
1, 5, and 10	Turbulency (LES), Lagrangian (DPM)	15, 30, and 60	17-generation anatomical model	ANSYS Fluent	-	Aerosols move in the deeper parts of the airways using a parabolic inlet velocity field	[26]

Table III (continued)

particle size (μm)	CFD model	Flow rate (L/min)	Realistic Geometry	Modeling platform	Experimental method	Main objective	Ref
1, 3, and 7	Turbulency (RANS k-ω-SST)	7.5 and 15	Throat, trachea and tracheobronchial tree	STAR-CCM +	Phase Doppler Anemometry, human airways cast	Numerical study of inspiratory airflow compared with experimental data using dynamic inhalation maneuvers	[42]
1.0, 2.5, 5.5, 8.5, and 10.0	Turbulency (RANS Realizable k- ε), Lagrangian (DPM)	PIFR: 81.8	Extra-thoracic, trachea, and bronchial airways	STAR-CCM +	-	Particles are released from an inlet using a time-dependent source function in the airways of COPD patients with varying severity	[31]
0.1, 0.5, 1, 2.5, 5 and 10	Turbulency (LES), Lagrangian	4.5, 15.2, 30, 60	Mouth, the oropharynx, the laryngopharynx, the larynx, the trachea, and the intra-thoracic airways	OpenFOAM	Laser Doppler Anemometry	Numerical analysis of electrostatically charged aerosol delivery with experimentally determined realistic inlet profile	[38]
1, 2, 4, 6, 8, and 10	Turbulency (LES), Lagrangian (DPM)	30 and 60	Extra-thoracic and tracheobronchial tree	OpenFOAM	-	Studying regional aerosol deposition affected by the mouth and throat using a cost-efficient approach	[57]
0.005, 0.1, 0.5, 1, 5 and 10	Turbulency (RANS Realizable k- ε), Lagrangian (DPM)	15 and 60	Mouth–throat and tracheobronchial	ANSYS Fluent	-	Investigating particle transport at nanoscale and microscale levels with and without stenosis and analyzing the roles of impaction and diffusion mechanisms	[46]
0.5–6.5	Turbulency (RANS LRN k-ω), Lagrangian (DPM)	14	Endotracheal tube or mouth–throat and tracheobronchial tree	ANSYS CFX	*In vitro* NGI	Studying aerosol characteristics and delivery using an adult ventilator circuit to a patient's specific lung airway and comparing the findings with experimental data	[30]
2.5, 5, and 10	Turbulency (RANS standard k-ω), Lagrangian (DPM)	7.5, 15, and 30	Mouth–throat, upper airway	ANSYS Fluent	-	Analyzing aerosol transport and deposition in stenosis airways	[40]

PIFR: Peak Inspiratory Flow Rate; NGI: Next Generation Impactor; DPM: discrete phase model

medication deposition in affected regions [204]. ML (machine learning) techniques (e.g., SVMs, ANNs, CNNs, NLP) support tasks like classification, regression, and segmentation [205–212]. Future work should explore conversational AI for patient interaction, enhancing image and sound processing techniques, and utilizing underexplored data sources.

Conclusion

Understanding the dynamics and deposition of aerosol particles in the pulmonary pathways is essential for assessing health risks and evaluating the effectiveness of drugs delivered to the lungs. Consequently, CFD simulations of aerosol medication delivery and deposition have been a key area of research over the past two decades. The evidence in this review demonstrates that *in silico* simulations can accurately assess and predict aerosol deposition patterns in the respiratory system, improving the precision of drug inhalation treatments. This paper reviews numerical modeling of pulmonary drug delivery from mouth to lungs, covering governing equations, forces, boundary conditions, lung geometry effects, powder characteristics, and validation with *in vitro*/*in vivo* data.

Aerosol drugs are typically delivered orally to improve lung penetration and therapeutic efficacy. Both 1-D and 3-D CFD models aid in understanding aerosol transport. While 1-D models simplify airway geometry and flow dynamics, they overlook key deposition factors. In contrast, 3-D CFD simulations account for breathing patterns, aerosol properties, wall interactions, and dynamic geometries—realistic or idealized—via numerical particle and airflow solutions.

Aerosol dose deposition in the lungs can be evaluated using *in vivo*, *in vitro*, or *in silico* approaches. *In vivo* methods are commonly used to assess drug delivery effectiveness but are limited by high costs, labor-intensive aerosol labelling, technical challenges, low resolution, and radiation risks. *In vitro* experiments use human airway models to study aerosol deposition but are costly and provide limited detail, especially for small airway structures where airflow is hard to measure. Due to the lungs'complex structure and challenges in measuring local deposition, there remains a lack of direct correlation between *in vitro* and *in vivo* aerosol inhalation studies.

In silico methods offer a practical way to assess aerosol flow and deposition in hard-to-reach lung areas. These methods incorporate variations in lung geometry, breathing patterns, and aerosol properties into CFD models, providing a fast, cost-effective, and non-invasive approach with significant clinical benefits for treating respiratory diseases like asthma and COPD. CFD models calculate airflow fields with laminar and turbulent flows by solving Navier–Stokes equations. Most simulations use RANS methods with turbulence models, typically favoring the k-ω-SST model. However, LES models are gaining popularity due to reduced computational costs compared to DNS, though their use in inhaler analysis remains limited. As computing power advances, DNS will allow more precise simulations.

Numerical solutions of algebraic equations use spatial meshing and finite differences, such as Taylor series, to approximate derivatives. The Lagrangian framework models aerosols as discrete entities in a continuous flow, facilitating analysis of turbulence and wall interactions. Advances in computational tools have made CFD models, integrated with DPM and DEM, essential for predicting airflow, particle dynamics, and aerosol dispersion. Particle motion is governed by forces like drag and gravity, while others—Saffman lift, buoyancy, Basset force, Brownian motion, and virtual mass—are typically negligible for micron-sized particles.

Lung models are categorized as idealized for basic mechanics or realistic for detailed analyses. Advances in imaging have led to CT/MR-based models that capture the complex lung branches for enhanced *in vitro* (airway replicas) and CFD studies. Accurate lung physiology simulation requires setting the correct boundary conditions. Various methods for determining flow rate/velocity include constant peak inspiratory flow rate, velocity based on inlet radius, sinusoidal parabolic velocity profiles, and realistic time-based inhalation patterns.

Key factors influencing aerosol behavior and lung deposition include particle size, morphology, surface texture, density, moisture affinity, and crystalline structure. Deposition mechanisms include inertial impaction for particles sized 3–6μm, gravitational settling for particles 1–3μm, and Brownian motion for particles smaller than 1μm. Inertial impaction is the primary mechanism for deposition in the upper airways, while larger particles settle by gravity and smaller particles deposit via diffusion. Effective integration of *in silico* simulations with *in vivo* and *in vitro* experiments can lead to the development of new inhaler technologies and powder formulations.

Laser/Phase-Doppler anemometry or Magnetic Resonance Velocimetry can be used for experimental airspeed measurements at the mouthpiece outlet. The accuracy of CFD predictions depends on precise initial particle size distribution (PSD) calculations, underscoring the need to combine cascade impactors with computational methods. Interdisciplinary knowledge is essential for precise CFD studies of aerosol dynamics in the lungs. Limited CT scan detail has hindered research into aerosol behavior in the lower airways. Delivering drugs to the lungs using CFD incurs significant computational costs due to the complexity of airway structures, dynamic airflow, and aerosol mechanics, requiring extensive computational effort. Various simplifications have been employed to mitigate these challenges.

The most frequently employed simplifications in scholarly works include the following:

- Current modeling often uses idealized or realistic geometry based on healthy individuals, neglecting to represent the diverse airway structures of patients with respiratory conditions and not considering differences in gender, age, height, and weight.
- Existing lung models, assuming rigid walls and static airways that ignore lung movement, lack physiological accuracy, and can't predict disease-specific airflow.
- Many studies assume a steady state condition or use constant inlet flow, which lowers the accuracy of deposition predictions. Realistic breathing simulations that reflect actual conditions as a time function are more accurate than the commonly used steady flow rate.
- Many studies only consider inhalation, omitting exhalation, yet both are vital for understanding respiratory mechanics. Furthermore, advised breath holding after inhalation is often disregarded in most CFD studies.
- Most studies tend to ignore the significance of the inhalation device, concentrating exclusively on examining the lungs. As a result, such research does not consider the possible drug loss in the capsule or the device or the potential reduction in airflow.
- One of the major hurdles faced by models in CFPD is their limited capacity to represent complex aerosol physics accurately. This encompasses particle collisions, electrostatic forces, and the condensation/evaporation or agglomeration/deagglomeration dynamics of particles.
- To fully grasp the process via CFD, accurate aerosol characterization is crucial. FPF, Mass MMAD, and density are key parameters that must be carefully assessed through *in vitro* studies, which are often overlooked
- In practice, most aerosol particles are not spherical, often taking on fiber-like, anisotropic shapes. However, CFD studies usually presume spherical shapes, resulting in discrepancies in the anticipated deposition patterns.
- Using RANS models over LES and DNS and omitting certain forces in Newton's law results in a less accurate representation of reality.

Simulations can provide precise and valuable results, including three-dimensional velocity and pressure profiles, as well as mean velocity measurements across key cross-sections. They can also demonstrate particle dispersion patterns in a 3D model, calculate DF and DE under various scenarios (such as changes in flow rate, air inlet patterns, pulmonary and particulate geometry, and different forces), and allow for comparison with empirical laboratory data.

We hope the data presented in this review will serve as a useful resource for identifying pulmonary conditions and mapping therapeutic aerosol deposition. This would represent a key step toward improving global health, reducing fatalities, and achieving the third Sustainable Development Goal.

Funding Funding for this study was provided by the Tabriz University of Medical Sciences, Tabriz, Iran (Grant No. 73544). We would like to express our appreciation for the cooperation of the Clinical Research Development Unit of Imam Reza General Hospital, Tabriz, Iran, in conducting this research.

Declarations

Conflict of interest The authors declare that they have no known competing financial interests or personal relationships that could have appeared to influence the work reported in this paper.

References

1. Islam MS, Saha SC, Sauret E, Ong H, Young P, Gu Y. Euler-Lagrange approach to investigate respiratory anatomical shape effects on aerosol particle transport and deposition. Toxicol Res Appl. 2019;3:239784731989467.
2. Chen J, Li C, Ristovski Z, Milic A, Gu Y, Islam MS, Wang S, Hao J, Zhang H, He C, Guo H. A review of biomass burning: emissions and impacts on air quality, health and climate in China. Sci Total Environ. 2017;579:1000–34.
3. Huang X, Saha SC, Saha G, Francis I, Luo Z. Transport and deposition of microplastics and nanoplastics in the human respiratory tract. Environ Adv. 2024;16:100525.
4. Islam MS, Larpruenrudee P, Hossain SI, Rahimi-Gorji M, Gu Y, Saha SC, Paul G. Polydisperse aerosol transport and deposition in upper airways of age-specific lung. Int J Environ Res Public Health. 2021;18(12):6239.
5. Zhao J, Feng Y, Koshiyama K, Wu H. Prediction of airway deformation effect on pulmonary air-particle dynamics: A numerical study. Phys Fluids. 2021;33(10).
6. Stein SW, Thiel CG. The History of Therapeutic Aerosols : A Chronological Review. 2017;30:20–41.
7. Owens DR, Zinman B, Bolli G. Alternative routes of insulin delivery. Diabet Med. 2003;20(11):886–98.
8. Ahookhosh K, Pourmehran O, Aminfar H, Mohammadpourfard M, Sarafraz MM, Hamishehkar H. Development of human respiratory airway models: A review. Eur J Pharm Sci. 2020;145:105233. https://doi.org/10.1016/j.ejps.2020.105233.
9. Salmanipour S, Sokhansanj A, Jafari N, Hamishehkar H, Saha SC. Engineering nanoliposomal tiotropium bromide embedded in a lactose-arginine carrier forming Trojan-particle dry powders for efficient pulmonary drug delivery: a combined approach of in vitro-3D printing and in silico-CFD modeling. Int J Pharm. 2025;671:125171.
10. Bhardwaj S, Koullapis P, Kassinos SC, Sznitman J. Fate of inhaled aerosols under the influence of glottal motion in a realistic in silico human tracheobronchial tree model. Eur J Pharm Sci. 2022;173:106172.
11. Capecelatro J, Longest W, Boerman C, Sulaiman M, Sundaresan S. Recent developments in the computational simulation of dry powder inhalers. Adv Drug Deliv Rev. 2022;188:114461. https://doi.org/10.1016/j.addr.2022.114461.
12. Salmanipour S, Sokhansanj A, Sarrafzadeh M, Akbari A. Using an anti-fouling electro- (stainless-steel/ PVC) membrane reactor in electrocoagulation process for arsenic removal: Experimental study and mechanism development in multiphase media using CFD. J Environ Chem Eng. 2023;11:111168. https://doi.org/10.1016/j.jece.2023.111168.

13. Longest PW, Holbrook LT. In silico models of aerosol delivery to the respiratory tract - Development and applications. Adv Drug Deliv Rev. 2012;64:296–311.
14. Ahookhosh K, Saidi M, Aminfar H, Mohammadpourfard M, Hamishehkar H, Yaqoubi S. Dry powder inhaler aerosol deposition in a model of tracheobronchial airways: Validating CFD predictions with in vitro data. Int J Pharm. 2020;587:119599. https://doi.org/10.1016/j.ijpharm.2020.119599.
15. Islam MS, Gu Y, Farkas A, Paul G, Saha SC. Helium–oxygen mixture model for particle transport in CT-based upper airways. Int J Environ Res Public Health. 2020;17(10):3574.
16. Longest PW, Tian G, Khajeh-Hosseini-Dalasm N, Hindle M. Validating whole-airway CFD predictions of DPI aerosol deposition at multiple flow rates. J Aerosol Med Pulm Drug Deliv. 2016;29:461–81.
17. Kolanjiyil AV, Kleinstreuer C, Sadikot RT. Computationally efficient analysis of particle transport and deposition in a human whole-lung-airway model. Part II: Dry powder inhaler application. Comput Biol Med. 2017;84:247–53. https://doi.org/10.1016/j.compbiomed.2016.10.025.
18. B Carrigy N, R Martin A, H Finlay W. Use of extrathoracic deposition models for patient-specific dose estimation during inhaler design. Curr Pharm Des. 2015;21(27):3984–92.
19. Kolanjiyil AV, Kleinstreuer C. Computational analysis of aerosol-dynamics in a human whole-lung airway model. J Aerosol Sci. 2017;114:301–16.
20. Huang F, Zhu Q, Zhou X, Gou D, Yu J, Li R, et al. Role of CFD based in silico modelling in establishing an in vitro-in vivo correlation of aerosol deposition in the respiratory tract. Adv Drug Deliv Rev. 2021;170:369–85. https://doi.org/10.1016/j.addr.2020.09.007.
21. Tian G, Hindle M, Lee S, Longest PW. Validating CFD Predictions of Pharmaceutical Aerosol Deposition with in Vivo Data. Pharm Res. 2015;32:3170–87.
22. Islam MS, Paul G, Ong HX, Young PM, Gu YT, Saha SC. A review of respiratory anatomical development, air flow characterization and particle deposition. Int J Environ Res Public Health. 2020;17(2):380.
23. Das P, Nof E, Amirav I, Kassinos SC, Sznitman J. Targeting inhaled aerosol delivery to upper airways in children: insight from computational fluid dynamics (CFD). PloS One. 2018;13(11):e0207711.
24. Sommerfeld M, Cui Y, Schmalfuß S. Potential and constraints for the application of CFD combined with Lagrangian particle tracking to dry powder inhalers. Eur J Pharm Sci. 2019;128:299–324. https://doi.org/10.1016/j.ejps.2018.12.008.
25. Kleinstreuer C. Modern fluid dynamics. Boca Raton, FL, USA: CRC Press; 2018.
26. Islam MS, Saha SC, Sauret E, Gemci T, Gu YT. Pulmonary aerosol transport and deposition analysis in upper 17 generations of the human respiratory tract. J Aerosol Sci. 2017;108:29–43.
27. Martin AR, Moore CP, Finlay WH. Models of deposition, pharmacokinetics, and intersubject variability in respiratory drug delivery. Expert Opin Drug Deliv. 2018;15:1175–88. https://doi.org/10.1080/17425247.2018.1544616.
28. Koullapis PG, Nicolaou L, Kassinos SC. In silico assessment of mouth-throat effects on regional deposition in the upper tracheobronchial airways. J Aerosol Sci. 2018;117:164–88. https://doi.org/10.1016/j.jaerosci.2017.12.001.
29. Koullapis PG, Hofemeier P, Sznitman J, Kassinos SC. An efficient computational fluid-particle dynamics method to predict deposition in a simplified approximation of the deep lung. Eur J Pharm Sci. 2018;113:132–44.
30. Rajendran RR, Kumaran S, Banerjee A, Berlinski A. A hybrid in vitro in silico framework for albuterol delivery through an adult ventilator circuit to a patient-specific lung airway model. J Aerosol Sci. 2021;158:1–21.
31. Kadota K, Matsumoto K, Uchiyama H, Tobita S, Maeda M, Maki D, et al. In silico evaluation of particle transport and deposition in the airways of individual patients with chronic obstructive pulmonary disease. Eur J Pharm Biopharm. 2022;174:10–9.
32. Xi J, Longest PW, Martonen TB. Effects of the laryngeal jet on nano-and microparticle transport and deposition in an approximate model of the upper tracheobronchial airways. J Appl Physiol. 2008;104(6):1761–77.
33. Delvadia RR, Longest PW, Hindle M, Byron PR. In vitro tests for aerosol deposition. III: effect of inhaler insertion angle on aerosol deposition. J Aerosol Med Pulm Drug Deliv. 2013;26(3):145–56.
34. Thomas ML, Longest PW. Evaluation of the polyhedral mesh style for predicting aerosol deposition in representative models of the conducting airways. J Aerosol Sci. 2022;159:1–17.
35. Cheng T, Carpenter D, Cohen S, Witsell D, Frank-Ito DO. Investigating the effects of laryngotracheal stenosis on upper airway aerodynamics. The Laryngoscope. 2018;128(4):E141–9.
36. Longest PW, Tian G, Delvadia R, Hindle M. Development of a stochastic individual path (SIP) model for predicting the deposition of pharmaceutical aerosols: effects of turbulence, polydisperse aerosol size, and evaluation of multiple lung lobes. Aerosol Sci Technol. 2012;46(12):1271–85.
37. Xi J, Longest PW. Transport and deposition of micro-aerosols in realistic and simplified models of the oral airway. Ann Biomed Eng. 2007;35(4):560–81.
38. Koullapis PG, Kassinos SC, Bivolarova MP, Melikov AK. Particle deposition in a realistic geometry of the human conducting airways: Effects of inlet velocity profile, inhalation flowrate and electrostatic charge. J Biomech. 2016;49:2201–12.
39. Medvedev AE, Fomin VM, Gafurova PS. Three-Dimensional Model of the Human Bronchial Tree—Modeling of the Air Flow in Normal and Pathological Cases. J Appl Mech Tech Phys. 2020;61:1–13.
40. Singh P, Raghav V, Padhmashali V, Paul G, Islam MS, Saha SC. Airflow and particle transport prediction through stenosis airways. Int J Environ Res Public Health. 2020;17(3):1119.
41. Ohsaki S, Mitani R, Fujiwara S, Nakamura H, Watano S. Effect of particle-wall interaction and particle shape on particle deposition behavior in human respiratory system. Chem Pharm Bull. 2019;67:1328–36.
42. Elcner J, Lizal F, Jedelsky J, Jicha M, Chovancova M. Numerical investigation of inspiratory airflow in a realistic model of the human tracheobronchial airways and a comparison with experimental results. Biomech Model Mechanobiol. 2016;15:447–69.
43. Bass K, Worth LP. Recommendations for simulating microparticle deposition at conditions similar to the upper airways with two-equation turbulence models. J Aerosol Sci. 2018;119:31–50.
44. Abolhassantash M, Tavakol MM, Abouali O, Yaghoubi M, Ahmadi G. Deposition fraction of ellipsoidal fibers in the human nasal cavity-Influence of non-creeping formulation of hydrodynamic forces and torques. Int J Multiphase Flow. 2020;126:103238.
45. Rahman MM, Zhao M, Islam MS, Dong K, Saha SC. Aging effects on airflow distribution and micron-particle transport and deposition in a human lung using CFD-DPM approach. Adv Powder Technol. 2021;32:3506–16. https://doi.org/10.1016/j.apt.2021.08.003.
46. Rahman MM, Zhao M, Islam MS, Dong K, Saha SC. Numerical study of nanoscale and microscale particle transport in realistic

lung models with and without stenosis. Int J Multiphase Flow. 2021;145:103842.
47. Kolanjiyil AV, Kleinstreuer C. Computational analysis of aerosol-dynamics in a human whole-lung airway model. J Aerosol Sci. 2017;114:301–16. https://doi.org/10.1016/j.jaerosci.2017.10.001.
48. Huang F, Zhang Y, Tong ZB, Chen XL, Yang RY, Yu AB. Numerical investigation of deposition mechanism in three mouth–throat models. Powder Technol. 2021;378:724–35.
49. Feng Y, Zhao J, Chen X, Lin J. An in silico subject-variability study of upper airway morphological influence on the airflow regime in a tracheobronchial tree. Bioeng. 2017;4(4):90.
50. Jubaer H, Thomas M, Farkas D, Kolanjiyil AV, Momin MA, Hindle M, Longest W. Development of an effective two-equation turbulence modeling approach for simulating aerosol deposition across a range of turbulence levels. J Aerosol Sci. 2024;175:106262.
51. Sommerfeld M, Sgrott Jr OL, Taborda MA, Koullapis P, Bauer K, Kassinos S. Analysis of flow field and turbulence predictions in a lung model applying RANS and implications for particle deposition. Eur J Pharm Sci. 2021;166:105959.
52. Arsalanloo A, Abbasalizadeh M, Khalilian M, Saniee Y, Ramezanpour A, Islam MS. A computational approach to understand the breathing dynamics and pharmaceutical aerosol transport in a realistic airways. Adv Powder Technol. 2022;33(7):103635.
53. Nicolaou L. Inertial and gravitational effects on aerosol deposition in the conducting airways. J Aerosol Sci. 2018;120:32–51.
54. Cui XG, Gutheil E. Large eddy simulation of the unsteady flowfield in an idealized human mouth–throat configuration. J Biomech. 2011;44(16):2768–74.
55. Cui X, Wu W, Gutheil E. Numerical study of the airflow structures in an idealized mouth-throat under light and heavy breathing intensities using large eddy simulation. Respir Physiol Neurobiol. 2018;248:1–9.
56. Cui X, Gutheil E. Three-dimensional unsteady large eddy simulation of the vortex structures and the mono-disperse particle dispersion in the idealized human upper respiratory system. J Aerosol Sci. 2017;114:195–208.
57. Koullapis PG, Nicolaou L, Kassinos SC. In silico assessment of mouth-throat effects on regional deposition in the upper tracheobronchial airways. J Aerosol Sci. 2018;117:164–88.
58. Islam MS, Saha SC, Gemci T, Yang IA, Sauret E, Gu YT. Polydisperse Microparticle Transport and Deposition to the Terminal Bronchioles in a Heterogeneous Vasculature Tree. Sci Rep. 2018;8:1–9.
59. Koullapis P, Kassinos SC, Muela J, Perez-Segarra C, Rigola J, Lehmkuhl O, et al. Regional aerosol deposition in the human airways: The SimInhale benchmark case and a critical assessment of in silico methods. Eur J Pharm Sci. 2018;113:77–94.
60. Ahookhosh K, Saidi M, Aminfar H, Mohammadpourfard M, Hamishehkar H, Yaqoubi S. Dry powder inhaler aerosol deposition in a model of tracheobronchial airways: validating CFD predictions with in vitro data. Int J Pharm. 2020;587:119599.
61. Wilcox DC. Turbulence modeling for CFD. La Canada, CA: DCW Industries; 1998.
62. Geronzi L, Fanni BM, De Jong B, Roest G, Kenjeres S, Celi S, Biancolini ME. A parametric 3D model of human airways for particle drug delivery and deposition. Fluids. 2024;9(1):27.
63. Haghnegahdar A, Zhao J, Feng Y. Lung aerosol dynamics of airborne influenza A virus-laden droplets and the resultant immune system responses: An in silico study. J Aerosol Sci. 2019;134:34–55. https://doi.org/10.1016/j.jaerosci.2019.04.009.
64. Smagorinsky J. General circulation experiments with the primitive equations: I. The basic experiment. Mon Weather Rev. 1963;91(3):99–164.
65. Lilly DK. A proposed modification of the Germano subgrid-scale eddy viscosity model. Phys. Fluids A. 1992;4(3):633–5.
66. Koullapis PG, Stylianou FS, Sznitman J, Olsson B, Kassinos SC. Towards whole-lung simulations of aerosol deposition: a model of the deep lung. J Aerosol Sci. 2020;144:105541.
67. Chalvatzaki E, Chatoutsidou SE, Lazaridis M. Simulations of the deposition of pharmaceutical aerosols in the human respiratory tract by dry powder inhalers (DPIs). J Drug Deliv Sci Technol. 2020;59:101915.
68. Kleinstreuer C, Zhang Z. Laminar-to-turbulent fluid-particle flows in a human airway model. Int J Multiphase Flow. 2003;29(2):271–89.
69. Nicolaou L, Zaki TA. Characterization of aerosol stokes number in 90° bends and idealized extrathoracic airways. J Aerosol Sci. 2016;102:105–27.
70. Longest PW, Xi J. Effectiveness of direct Lagrangian tracking models for simulating nanoparticle deposition in the upper airways. Aerosol Sci Technol. 2007;41(4):380–97.
71. Dehbi A. A CFD model for particle dispersion in turbulent boundary layer flows. Nucl Eng Des. 2008;238(3):707–15.
72. Islam MS, Saha SC, Sauret E, Gemci T, Yang IA, Gu YT. Ultrafine particle transport and deposition in a large scale 17-generation lung model. J Biomech. 2017;64:16–25.
73. Jayaraju ST, Brouns M, Verbanck S, Lacor C. Fluid flow and particle deposition analysis in a realistic extrathoracic airway model using unstructured grids. J Aerosol Sci. 2007;38(5):494–508.
74. Lambert AR, O'shaughnessy PT, Tawhai MH, Hoffman EA, Lin CL. Regional deposition of particles in an image-based airway model: large-eddy simulation and left-right lung ventilation asymmetry. Aerosol Sci Technol. 2011;45(1):11–25.
75. Li A, Ahmadi G. Dispersion and deposition of spherical particles from point sources in a turbulent channel flow. Aerosol Sci Technol. 1992;16(4):209–26.
76. Sommerfeld M. Validation of a stochastic Lagrangian modelling approach for inter-particle collisions in homogeneous isotropic turbulence. Int J Multiphase Flow. 2001;27(10):1829–58.
77. Xi J, Talaat M, Si XA. Two-way coupling and Kolmogorov scales on inhaler spray plume evolutions from Ventolin, ProAir, and Qvar. Math Biosci Eng. 2022;19:10915–40.
78. Haghnegahdar A, Zhao J, Kozak M, Williamson P, Feng Y. Development of a hybrid CFD-PBPK model to predict the transport of xenon gas around a human respiratory system to systemic regions. Heliyon. 2019;5(4).
79. Cundall PA, Strack OD. A discrete numerical model for granular assemblies. Geotechnique. 1979;29(1):47–65.
80. Zhu HP, Zhou ZY, Yang RY, Yu AB. Discrete particle simulation of particulate systems: a review of major applications and findings. Chem Eng Sci. 2008;63(23):5728–70.
81. Kwok PC, Glover W, Chan HK. Electrostatic charge characteristics of aerosols produced from metered dose inhalers. J Pharm Sci. 2005;94(12):2789–99.
82. Forsyth B, Liu BY, Romay FJ. Particle charge distribution measurement for commonly generated laboratory aerosols. Aerosol Sci Technol. 1998;28(6):489–501.
83. Young PM, Sung A, Traini D, Kwok P, Chiou H, Chan HK. Influence of humidity on the electrostatic charge and aerosol performance of dry powder inhaler carrier based systems. Pharm Res. 2007;24(5):963–70.
84. Kolehmainen J, Sippola P, Raitanen O, Ozel A, Boyce CM, Saarenrinne P, Sundaresan S. Effect of humidity on triboelectric charging in a vertically vibrated granular bed: experiments and modeling. Chem Eng Sci. 201714;173:363–73.
85. Beretta M, Hörmann TR, Hainz P, Hsiao WK, Paudel A. Investigation into powder tribo–charging of pharmaceuticals. Part II: sensitivity to relative humidity. Int J Pharm. 2020;591:120015.

86. Cui Y, Schmalfuß S, Zellnitz S, Sommerfeld M, Urbanetz N. Towards the optimisation and adaptation of dry powder inhalers. Int J Pharm. 2014;470(1–2):120–32.
87. Cui Y, Sommerfeld M. Application of Lattice-Boltzmann Method for Analysing Detachment of Micron-Sized Particles from Carrier Particles in Turbulent Flows. Flow, Turbul Combust. 2018;100:271–97.
88. Cui Y, Sommerfeld M. Forces on micron-sized particles randomly distributed on the surface of larger particles and possibility of detachment. Int J Multiphase Flow. 2015;72:39–52.
89. Maxey MR, Riley JJ. Equation of motion for a small rigid sphere in a nonuniform flow. The Phys Fluids. 1983;26(4):883–9.
90. Saffman PG. The lift on a small sphere in a slow shear flow. J Fluid Mech. 1965;22(2):385–400.
91. Ganser GH. A rational approach to drag prediction of spherical and nonspherical particles. Powder Technol. 1993;77(2):143–52.
92. Islam MS, Saha SC, Gemci T, Yang IA, Sauret E, Ristovski Z, et al. Euler-Lagrange Prediction of Diesel-Exhaust Polydisperse Particle Transport and Deposition in Lung: Anatomy and Turbulence Effects. Sci Rep. 2019;9:1–16.
93. Feng Y, Marchal T, Sperry T, Yi H. Influence of wind and relative humidity on the social distancing effectiveness to prevent COVID-19 airborne transmission: a numerical study. J Aerosol Sci. 2020;147:105585.
94. Newman SP, Pitcairn GR, Hirst PH, Bacon RE, O'keefe E, Reiners M, Hermann R. Scintigraphic comparison of budesonide deposition from two dry powder inhalers. Eur Respir J. 2000;16(1):178–83.
95. Tanprasert S, Kampeewichean C, Shiratori S, Piemjaiswang R, Chalermsinsuwan B. Non-spherical drug particle deposition in human airway using computational fluid dynamics and discrete element method. Int J Pharm. 2023;639:122979.
96. Comerford A, Förster C, Wall WA. Structured tree impedance outflow boundary conditions for 3D lung simulations. J Biomech Eng. 2010;132(8):081002.
97. Yin Y, Choi J, Hoffman EA, Tawhai MH, Lin CL. Simulation of pulmonary air flow with a subject-specific boundary condition. J Biomech. 2010;43(11):2159–63.
98. Hofmann W, Sturm R. Stochastic model of particle clearance in human bronchial airways. J Aerosol Med. 2004;17(1):73–89.
99. Longest PW, Bass K, Dutta R, Rani V, Thomas ML, El-Achwah A, et al. Use of computational fluid dynamics deposition modeling in respiratory drug delivery. Expert Opin Drug Deliv. 2019;16:7–26. https://doi.org/10.1080/17425247.2019.1551875.
100. Sosnowski TR. Towards more precise targeting of inhaled aerosols to different areas of the respiratory system. Pharm. 2024;16(1):97.
101. Ennis BJ, Tardos G, Pfeffer R. A microlevel-based characterization of granulation phenomena. Powder Techno. 1991;65(1–3):257–72.
102. Rahimi-Gorji M, Gorji TB, Gorji-Bandpy M. Details of regional particle deposition and airflow structures in a realistic model of human tracheobronchial airways: two-phase flow simulation. Comput Biol Med. 2016;74:1–7.
103. Ferron GA, Upadhyay S, Zimmermann R, Karg E. Model of the deposition of aerosol particles in the respiratory tract of the rat. II: hygroscopic particle deposition. J Aerosol Med Pulm Drug Deliv. 2013;26(2):101–19.
104. Worth Longest P, Xi J. Condensational growth may contribute to the enhanced deposition of cigarette smoke particles in the upper respiratory tract. Aerosol Sci Technol. 2008;42(8):579–602.
105. Choi JI, Kim CS. Mathematical analysis of particle deposition in human lungs: an improved single path transport model. Inhal toxicol. 2007;19(11):925–39.
106. Martonen TB. Analytical model of hygroscopic particle behavior in human airways. Bull Math Biol. 1982;44(3):425–42.
107. Longest PW, Hindle M, Choudhuri SD, Xi J. Comparison of ambient and spray aerosol deposition in a standard induction port and more realistic mouth–throat geometry. J Aerosol Sci. 2008;39(7):572–91.
108. Longest PW, Hindle M. Evaluation of the Respimat Soft Mist inhaler using a concurrent CFD and in vitro approach. J Aerosol Med Pulm Drug Deliv. 2009;22(2):99–112.
109. Bui VK, Moon JY, Chae M, Park D, Lee YC. Prediction of aerosol deposition in the human respiratory tract via computational models: a review with recent updates. Atmos. 2020;11(2):137.
110. Hofmann W, Koblinger L. Monte Carlo modeling of aerosol deposition in human lungs. Part II: deposition fractions and their sensitivity to parameter variations. J Aerosol Sci. 1990;21(5):675–88.
111. Hofmann W, Asgharian B, Winkler-Heil R. Modeling intersubject variability of particle deposition in human lungs. J Aerosol Sci. 2002;33(2):219–35.
112. Hofmann W, Bergmann R, Koblinger L. Characterization of local particle deposition patterns in human and rat lungs by different morphometric parameters. J Aerosol Sci. 1999;30(5):651–67.
113. Hofmann W, Bolt L, Sturm R, Fleming JS, Conway JH. Simulation of three-dimensional particle deposition patterns in human lungs and comparison with experimental SPECT data. Aerosol Sci Technol. 2005;39(8):771–81.
114. Person A, Mintz ML. Anatomy and physiology of the respiratory tract. In disorders of the respiratory tract: common challenges in primary care. Totowa, NJ: Humana Press; 2006. p. 11–15.
115. Kleinstreuer C, Zhang Z, Donohue JF. Targeted drug-aerosol delivery in the human respiratory system. Annu Rev Biomed Eng. 2008;10(1):195–220.
116. Hofmann W. Modelling inhaled particle deposition in the human lung—a review. J Aerosol Sci. 2011;42(10):693–724.
117. Kleinstreuer C, Zhang Z. Airflow and particle transport in the human respiratory system. Ann Rev Fluid Mech. 2010;42(1):301–34.
118. Lin CL, Tawhai MH, McLennan G, Hoffman EA. Characteristics of the turbulent laryngeal jet and its effect on airflow in the human intra-thoracic airways. Respir Physiol Neurobiol. 2007;157(2–3):295–309.
119. Feng Y, Zhao J, Kleinstreuer C, Wang Q, Wang J, Wu DH, et al. An in silico inter-subject variability study of extra-thoracic morphology effects on inhaled particle transport and deposition. J Aerosol Sci. 2018;123:185–207.
120. Zhou Y, Sun J, Cheng YS. Comparison of deposition in the USP and physical mouth–throat models with solid and liquid particles. J Aerosol Med Pulm Drug Deliv. 2011;24(6):277–84.
121. Tang P, Kwok PC, Tong Z, Yang R, Raper JA, Chan HK. Does the United States Pharmacopeia throat introduce de-agglomeration of carrier-free powder from inhalers?. Pharm Res. 2012;29(7):1797–807.
122. Yousefi M, Pourmehran O, Gorji-Bandpy M, Inthavong K, Yeo L, Tu J. CFD simulation of aerosol delivery to a human lung via surface acoustic wave nebulization. Biomech Model Mechanobiol. 2017;16(6):2035–50.
123. Bordas R, Lefevre C, Veeckmans B, Pitt-Francis J, Fetita C, Brightling CE, Kay D, Siddiqui S, Burrowes KS. Development and analysis of patient-based complete conducting airways models. PloS One. 2015;10(12):e0144105.
124. Koullapis P, Stylianou F, Lin CL, Kassinos S, Sznitman J. In silico methods to model dose deposition. In Inhaled Medicines. Academic Press; 2021. p. 167–195.

125. Hansen JE, Ampaya EP. Human air space shapes, sizes, areas, and volumes. J Appl Physiol. 1975;38(6):990–5.
126. Weibel ER. Geometric and dimensional airway models of conductive, transitory and respiratory zones of the human lung. In Morphometry of the human lung. Berlin, Heidelberg: Springer; 1963. p. 136–142.
127. Tu J, Inthavong K, Ahmadi G. Computational fluid and particle dynamics in the human respiratory system. Springer Science & Business Media; 2012.
128. Sznitman J, Heimsch F, Heimsch T, Rusch D, Rösgen T. Three-dimensional convective alveolar flow induced by rhythmic breathing motion of the pulmonary acinus.
129. Kolanjiyil AV, Kleinstreuer C. Modeling airflow and particle deposition in a human acinar region. Comput Math Methods Med. 2019;2019(1):5952941.
130. Islam MR, Larpruenrudee P, Rahman MM, Ullah S, Godder TK, Cui X, Mortazavy Beni H, Inthavong K, Dong J, Gu Y, Islam MS. How nanoparticle aerosols transport through multi-stenosis sections of upper airways: a CFD-DPM modelling. Atmos. 2022;13(8):1192.
131. Weibel ER, Cournand AF, Richards DW. Morphometry of the human lung. Berlin: Springer; 1963.
132. Horsfield K, Dart G, Olson DE, Filley GF, Cumming G. Models of the human bronchial tree. J Appl Physiol. 1971;31(2):207–17.
133. Ball L, Vercesi V, Costantino F, Chandrapatham K, Pelosi P. Lung imaging: how to get better look inside the lung. Ann Transl Med. 2017;5(14):294.
134. Beni HM, Mortazavi H, Islam MS. Biomedical and biophysical limits to mathematical modeling of pulmonary system mechanics: a scoping review on aerosol and drug delivery. Biomech Model Mechanobiol. 2022;21:79–87. https://doi.org/10.1007/s10237-021-01531-8.
135. Longest PW, Tian G, Walenga RL, Hindle M. Comparing MDI and DPI aerosol deposition using in vitro experiments and a new stochastic individual path (SIP) model of the conducting airways. Pharm Res. 2012;29(6):1670–88.
136. Katz IM, Martin AR, Muller PA, Terzibachi K, Feng CH, Caillibotte G, Sandeau J, Texereau J. The ventilation distribution of helium–oxygen mixtures and the role of inertial losses in the presence of heterogeneous airway obstructions. Journal of Biomech. 2011;44(6):1137–43.
137. Bass K, Boc S, Hindle M, Dodson K, Longest W. High-Efficiency Nose-to-Lung Aerosol Delivery in an Infant: Development of a Validated Computational Fluid Dynamics Method. J Aerosol Med Pulm Drug Deliv. 2019;32:132–48.
138. Gu Q, Qi S, Yue Y, Shen J, Zhang B, Sun W, et al. Structural and functional alterations of the tracheobronchial tree after left upper pulmonary lobectomy for lung cancer. Biomed Eng Online. 2019;18:105. https://doi.org/10.1186/s12938-019-0722-6.
139. Farkas Á, Lizal F, Jedelsky J, Elcner J, Karas J, Belka M, Misik O, Jicha M. The role of the combined use of experimental and computational methods in revealing the differences between the micron-size particle deposition patterns in healthy and asthmatic subjects. J Aerosol Sci. 2020;147:105582.
140. Farkas Á, Lizal F, Jedelsky J, Elcner J, Horváth A, Jicha M. Simulation of airway deposition of an aerosol drug in COPD patients. Pharm. 2019;11(4):153.
141. Cebral JR, Summers RM. Tracheal and central bronchial aerodynamics using virtual bronchoscopy and computational fluid dynamics. IEEE Trans Med Imaging. 2004;23(8):1021–33.
142. Griscom NT, Wohl ME. Dimensions of the growing trachea related to age and gender. Am J Roentgenol. 1986;146(2):233–7.
143. Hofmann W. Mathematical model for the postnatal growth of the human lung. Respir Physiol. 1982;49(1):115–29.
144. Amirav I, Newhouse MT. Aerosol therapy in infants and toddlers: past, present and future. Expert Rev Respir Med. 2008;2(5):597–605.
145. Asgharian B, Menache MG, Miller FJ. Modeling age-related particle deposition in humans. J Aerosol Med. 2004;17(3):213–24.
146. Niewoehner DE, Kleinerman J. Morphologic basis of pulmonary resistance in the human lung and effects of aging. J Appl Physiol. 1974;36(4):412–8.
147. Rahman MM, Zhao M, Islam MS, Dong K, Saha SC. Aging effects on airflow distribution and micron-particle transport and deposition in a human lung using CFD-DPM approach. Adv Powder Technol. 2021;32:3506–16.
148. Newman SP. Drug delivery to the lungs: challenges and opportunities. Ther Deliv. 2017;8(8):647–61.
149. Xi J, Talaat M, Si XA, Han P, Dong H, Zheng S. Alveolar size effects on nanoparticle deposition in rhythmically expanding-contracting terminal alveolar models. Comput Biol Med. 2020;121:103791. https://doi.org/10.1016/j.compbiomed.2020.103791.
150. Xi J, Talaat M, Si XA, Chandra S. The application of statistical shape modeling for lung morphology in aerosol inhalation dosimetry. J Aerosol Sci. 2021;151:105623. https://doi.org/10.1016/j.jaerosci.2020.105623.
151. Talaat M, Si X, Xi J. Adjoint solver-based analysis of mouth–tongue morphologies on vapor deposition in the upper airway. Fluids. 2024;9(5):104.
152. Dominelli PB, Ripoll JG, Cross TJ, Baker SE, Wiggins CC, Welch BT, Joyner MJ. Sex differences in large conducting airway anatomy. J Appl Physiol. 2018;125(3):960–5.
153. Zhang Z, Kleinstreuer C. Laminar-to-turbulent fluid–nanoparticle dynamics simulations: Model comparisons and nanoparticle-deposition applications. Int J Numer Method Biomed Eng. 2011;27(12):1930–50.
154. Chen X, Feng Y, Zhong W, Kleinstreuer C. Numerical investigation of the interaction, transport and deposition of multicomponent droplets in a simple mouth-throat model. J Aerosol Sci. 2017;105:108–27.
155. Haber S, Yitzhak D, Tsuda A. Gravitational deposition in a rhythmically expanding and contracting alveolus. J Appl Physiol. 2003;95:657–71.
156. Kolanjiyil AV, Kleinstreuer C. Computationally efficient analysis of particle transport and deposition in a human whole-lung-airway model. Part I: Theory and model validation. Comput Biol Med. 2016;79:193–204. https://doi.org/10.1016/j.compbiomed.2016.10.020.
157. Weers JG, Miller DP. Formulation design of dry powders for inhalation. J Pharm Sci. 2015;104(10):3259–88.
158. Longest W, Hassan A, Farkas D, Hindle M. Computational Fluid Dynamics (CFD) Guided Spray Drying Recommendations for Improved Aerosol Performance of a Small-Particle Antibiotic Formulation. Pharm Res. 2022;39:295–316.
159. Longest PW, Farkas D, Hassan A, Hindle M. Computational fluid dynamics (CFD) simulations of spray drying: linking drying parameters with experimental aerosolization performance. Pharm Res. 2020;37(6):101.
160. Peng T, Lin S, Niu B, Wang X, Huang Y, Zhang X, Li G, Pan X, Wu C. Influence of physical properties of carrier on the performance of dry powder inhalers. Acta Pharm Sin B. 2016;6(4):308–18.
161. Longest W, Farkas D, Bass K, Hindle M. Use of Computational Fluid Dynamics (CFD) Dispersion Parameters in the Development of a New DPI Actuated with Low Air Volumes. Pharm Res. 2019;36:1–17.
162. Cheng YS. Mechanisms of pharmaceutical aerosol deposition in the respiratory tract. AAPS Pharmscitech. 2014;15(3):630–40.

163. Farkas Á, Balásházy I. Quantification of particle deposition in asymmetrical tracheobronchial model geometry. Comput Biol Med. 2008;38(4):508–18.
164. Miravitlles M, Auladell-Rispau A, Monteagudo M, Vázquez-Niebla JC, Mohammed J, Nuñez A, Urrútia G. Systematic review on long-term adverse effects of inhaled corticosteroids in the treatment of COPD. Eur Respir Rev. 2021;30(160).
165. Shekunov BY, Chattopadhyay P, Tong HH, Chow AH. Particle size analysis in pharmaceutics: principles, methods and applications. Pharm Res. 2007;24(2):203–27.
166. Watling CP, Elliott JA, Scruton C, Cameron RE. Surface modification of lactose inhalation blends by moisture. Int J Pharm. 2010;391(1–2):29–37.
167. Faulhammer E, Zellnitz S, Wutscher T, Stranzinger S, Zimmer A, Paudel A. Performance indicators for carrier-based DPIs: carrier surface properties for capsule filling and API properties for in vitro aerosolisation. Int J Pharm. 2018;536(1):326–35.
168. Kwok PC, Chan HK. Effect of relative humidity on the electrostatic charge properties of dry powder inhaler aerosols. Pharm Res. 2008;25(2):277–88.
169. Zhou QT, Morton DA. Drug–lactose binding aspects in adhesive mixtures: controlling performance in dry powder inhaler formulations by altering lactose carrier surfaces. Adv Drug Deliv Rev. 2012;64(3):275–84.
170. Sou T, Kaminskas LM, Nguyen TH, Carlberg R, McIntosh MP, Morton DA. The effect of amino acid excipients on morphology and solid-state properties of multi-component spray-dried formulations for pulmonary delivery of biomacromolecules. Eur J Pharm Biopharm. 2013;83(2):234–43.
171. Shukla SK, Sarode A, Kanabar DD, Muth A, Kunda NK, Mitragotri S, Gupta V. Bioinspired particle engineering for non-invasive inhaled drug delivery to the lungs. Mater Sci Eng C. 2021;128:112324.
172. Kaialy W, Alhalaweh A, Velaga SP, Nokhodchi A. Effect of carrier particle shape on dry powder inhaler performance. Int J Pharm. 2011;421(1):12–23.
173. Wan KY, Weng J, Wong SN, Kwok PC, Chow SF, Chow AH. Converting nanosuspension into inhalable and redispersible nanoparticles by combined in-situ thermal gelation and spray drying. Eur J Pharm Biopharm. 2020;149:238–47.
174. Secolin VA, Souza CRF, Oliveira WP. Spray drying of lipid-based systems loaded with Camellia sinensis polyphenols. J Liposome Res. 2017;27:11–20.
175. Lakio S, Morton DAV, Ralph AP, Lambert P. Optimizing aerosolization of a high-dose L-arginine powder for pulmonary delivery. Asian J Pharm Sci. 2015;10:528–40. https://doi.org/10.1016/j.ajps.2015.08.001.
176. Seville PC, Learoyd TP, Li HY, Williamson IJ, Birchall JC. Amino acid-modified spray-dried powders with enhanced aerosolisation properties for pulmonary drug delivery. Powder Technol. 2007;178:40–50.
177. Gradon L, Sosnowski TR. Formation of particles for dry powder inhalers. Adv Powder Technol. 2014;25(1):43–55.
178. Islam N, Stewart P, Larson I, Hartley P. Surface roughness contribution to the adhesion force distribution of salmeterol xinafoate on lactose carriers by atomic force microscopy. J Pharm Sci. 2005;94(7):1500–11.
179. Chew NY, Tang P, Chan HK, Raper JA. How much particle surface corrugation is sufficient to improve aerosol performance of powders?. Pharm Res. 2005;22(1):148–52.
180. Broday DM, Georgopoulos PG. Growth and deposition of hygroscopic particulate matter in the human lungs. Aerosol Sci Technol. 2001;34(1):144–59.
181. Asgharian B, Anjilvel S. A multiple-path model of fiber deposition in the rat lung. Toxicol Sci. 1998;44(1):80–6.
182. Alipour N, Salmanipour S, Rezaie A, Amini H, Ghahremaninasab M, Mehdipour A, et al. Mussel-inspired modified regenerated cellulose as tissue adhesive and antibacterial gauze : A promising approach for rapid hemostasis in non-compressible hemorrhage. Carbohydr Polym. 2025;349:122949. https://doi.org/10.1016/j.carbpol.2024.122949.
183. Alipour N, Jarolmasjed S, Salmanipour S, Rezaie A, Ghahremani-Nasab M, Milani M, et al. Dual Functionalized Absorbable Hairy Cellulose-Based Fabric for Efficient Hemostasis and Antibacterial Property. Adv Healthc Mater. 2025;2404438:1–23.
184. Conway J. Lung imaging—two dimensional gamma scintigraphy, SPECT, CT and PET. Adv Drug Deliv Rev. 2012;64(4):357–68.
185. Newman S, Steed K, Hooper G, Källén A, Borgström L. Comparison of gamma scintigraphy and a pharmacokinetic technique for assessing pulmonary deposition of terbutaline sulphate delivered by pressurized metered dose inhaler. Pharm Res. 1995;12(2):231–6.
186. Srichana T, Suedee R, Muanpanarai D, Tanmanee N. The study of in vitro–in vivo correlation: pharmacokinetics and pharmacodynamics of albuterol dry powder inhalers. J Pharm Sci. 2005;94(1):220–30.
187. Srichana T, Suedee R, Tanmanee N, Muanpanarai D, Marriott C. The correlation of urinary levels of albuterol and its metabolites isomers following inhalation from a dry powder inhaler and in vitro particle size characterisation. Pulm Pharmacol Ther. 2007;20(1):36–45.
188. Fleming JS, Conway JH, Bolt L, Holgate ST. A comparison of planar scintigraphy and SPECT measurement of total lung deposition of inhaled aerosol. J Aerosol Med. 2003;16(1):9–19.
189. Fleming JS, Epps BP, Conway JH, Martonen TB. Comparison of SPECT aerosol deposition data with a human respiratory tract model. J Aerosol Med. 2006;19(3):268–78.
190. Olsson B, Borgström L, Lundbäck H, Svensson M. Validation of a general in vitro approach for prediction of total lung deposition in healthy adults for pharmaceutical inhalation products. J Aerosol Med Pulm Drug Deliv. 2013;26(6):355–69.
191. Phalen RF, Yeh HC, Raabe OG, Velasquez DJ. Casting the lungs in-situ. The Anat Rec. 1973;177(2):255–63.
192. Dunbar CA, Watkins AP, Miller JF. An experimental investigation of the spray issued from a pMDI using laser diagnostic techniques. J Aerosol Med. 1997;10(4):351–68.
193. Banko AJ, Coletti F, Schiavazzi D, Elkins CJ, Eaton JK. Three-dimensional inspiratory flow in the upper and central human airways. Exp Fluids. 2015;56(6):117.
194. Van de Moortele T, Wendt CH, Coletti F. Morphological and functional properties of the conducting human airways investigated by in vivo computed tomography and in vitro MRI. J Appl Physiol. 2018;124(2):400–13.
195. Longest PW, Son YJ, Holbrook L, Hindle M. Aerodynamic factors responsible for the deaggregation of carrier-free drug powders to form micrometer and submicrometer aerosols. Pharm Res. 2013;30(6):1608–27.
196. Newman SP, Chan HK. In vitro-in vivo correlations (IVIVCs) of deposition for drugs given by oral inhalation. Adv Drug Deliv Rev. 2020;167:135–47.
197. Mitchell J, Newman S, Chan HK. In vitro and in vivo aspects of cascade impactor tests and inhaler performance: a review. Aaps Pharmscitech. 2007;8(4):110.
198. Littringer EM, Mescher A, Schroettner H, Achelis L, Walzel P, Urbanetz NA. Spray dried mannitol carrier particles with tailored surface properties–The influence of carrier surface roughness and shape. Eur J Pharm Biopharm. 2012;82(1):194–204.
199. Mitani R, Ohsaki S, Nakamura H, Watano S. Numerical study on particle adhesion in dry powder inhaler device. Chem Pharml Bull. 2020;68(8):726–36.

200. Copleyscientific. Available from: https://www.copleyscientific.com/inhaler-testing/aerodynamic-particle-size-distribution-apsd/apsd-of-aqueous-droplet-inhalers-adis/adis/
201. Zhao J, Feng Y, Tian G, Taylor C, Arden NS. Influences of puff protocols and upper airway anatomy on cannabis pharmacokinetics: a CFPD-PK study. Comput Biol Med. 2021;132:104333.
202. Rebello J, Brashier B, Shukla S. Assessment of the predictive capability of modelling and simulation to determine bioequivalence of inhaled drugs: A systematic review. DARU, J Pharm Sci. 2022;30:229–43. https://doi.org/10.1007/s40199-021-00423-7.
203. Dutta R, Kolanjiyil AV, Walenga RL, Chopski SG, Kaviratna A, Mohan AR, Newman B, Golshahi L, Longest W. CFD-PK model for nasal suspension sprays: validation with human adult in vivo data for triamcinolone acetonide. Int J Pharm. 2024;665:124660.
204. Talaat M, Xi J, Tan K, Si XA, Xi J. Convolutional neural network classification of exhaled aerosol images for diagnosis of obstructive respiratory diseases. J Nanotheranostics. 2023;4(3):228–47.
205. Xi J, Kim J, Si XA, Corley RA, Kabilan S, Wang S. CFD modeling and image analysis of exhaled aerosols due to a growing bronchial tumor: towards non-invasive diagnosis and treatment of respiratory obstructive diseases. Theranostics. 2015;5(5):443.
206. Zheng H, Hu Y, Dong L, Shu Q, Zhu M, Li Y, Chen C, Gao H, Yang L. Predictive diagnosis of chronic obstructive pulmonary disease using serum metabolic biomarkers and least-squares support vector machine. J Clin Lab Anal. 2021;35(2):e23641.
207. Sun J, Liao X, Yan Y, Zhang X, Sun J, Tan W, Liu B, Wu J, Guo Q, Gao S, Li Z. Detection and staging of chronic obstructive pulmonary disease using a computed tomography–based weakly supervised deep learning approach. Eur Radiol. 2022;32(8):5319–29.
208. Zou X, Ren Y, Yang H, Zou M, Meng P, Zhang L, Gong M, Ding W, Han L, Zhang T. Screening and staging of chronic obstructive pulmonary disease with deep learning based on chest X-ray images and clinical parameters. BMC Pulm Med. 2024;24(1):153.
209. Shah-Mohammadi F, Finkelstein J. NLP-assisted differential diagnosis of chronic obstructive pulmonary disease exacerbation. In Med Info; 2023 p. 589–593.
210. Idrisoglu A, Dallora AL, Cheddad A, Anderberg P, Jakobsson A, Berglund JS. COPDVD: automated classification of chronic obstructive pulmonary disease on a new collected and evaluated voice dataset. Artif Intell Med. 2024;156:102953.
211. Khademi S, Palmer C, Javed M, Dimaguila GL, Buttery JP, Black J. Detecting asthma presentations from emergency department notes: an active learning approach. In Australasian conference on data science and machine learning. Singapore: Springer; 2023. p. 284–298.
212. Salmani Pour Avval S, Eskue ND, Groves RM, Yaghoubi V. Systematic review on neural architecture search. Artif Intell Rev. 2025;58(3):73.